J. Appl. Cryst. (1988). **21**, 285–304

Some Basic Concepts of Texture Analysis and Comparison of Three Methods to Calculate Orientation Distributions from Pole Figures

By S. Matthies

Akademie der Wissenschaften, Zentralinstitut für Kernforschung Rossendorf, 8051 *Dresden, German Democratic Republic*

H.-R. Wenk

Department of Geology and Geophysics, University of California, Berkeley, CA 94720, *USA*

and G. W. Vinel

Akademie der Wissenschaften, Zentralinstitut für Kernforschung Rossendorf, 8051 *Dresden, German Democratic Republic*

(*Received* 3 *September* 1987; *accepted* 9 *February* 1988)

Abstract

Several methods have been developed which derive the orientation distribution (ODF) in a polycrystalline sample from pole figures measured by X-ray or neutron diffraction techniques. The theoretical backgrounds of the conventional harmonic method, of the vector method and of the method of Williams [*J. Appl. Phys.* (1968). **39**, 4329–4335], Imhof [*Textures Microstruct.* (1982). **5**, 73–86] and Matthies & Vinel [*Phys. Status Solidi B* (1982). **112**, K111–K120] (WIMV) are reviewed. A quantitative comparison is then made using the same input data and the same computer to evaluate resolution, errors and efficiency. The input data consist of standard functions, Taylor predictions and measured pole figures covering a realistic range of possibilities for both cubic and trigonal crystal symmetries. Comprehensive error criteria are introduced, and it is proposed to use both integral errors (RP) and difference pole figures to assess the quality of the pole-figure inversion. The harmonic method and WIMV are able to reproduce the original pole figures from the ODF within computer roundoff errors. Resolution of the vector method, particularly for low crystal symmetry, is considerably worse owing to the large-volume cells in orientation space. Computing time is optimal for the conventional harmonic method (for medium termination L), slightly worse for WIMV and about an order of magnitude higher for the vector method. Whereas the conventional harmonic method only reproduces the ghost-afflicted part $\tilde{f}(g)$ of the ODF, the vector method satisfies automatically the non-negativity criterion; however, only WIMV provides a general (conditional) ghost correction. In the examples chosen the ghost-corrected ODF $f(g)$ closely coincides with the starting model (model with standard functions or Taylor prediction) supporting its physical relevance. An attractive feature of WIMV is that it leads to results of satisfactory quality using fewer pole figures than the harmonic method. This is particularly important for low crystal symmetries. Furthermore, the treatment of incomplete pole figures is straightforward.

1. Introduction

The goal of quantitative texture analysis is to determine the orientation distribution of crystallites (ODF – orientation distribution function) in a polycrystalline aggregate, to interpret this distribution in terms of processes which lead to its formation, and to establish a relationship between the ODF and macroscopic properties (Wassermann & Grewen, 1962; Bunge, 1969; Wenk, 1985). In recent years some fundamental problems in connection with the determination of the ODF from pole figures were discovered (Bunge & Esling, 1982; Jura, Pospiech & Lücke, 1980; Matthies, 1979, 1980*a*, 1982*a*, 1984; Matthies & Helming, 1982). These were most clearly revealed with ‘standard functions’ (Matthies, 1980*b*, 1982*b*; Matthies, Vinel & Helming, 1987) which documented the difficulty of ghosts and provided the framework for a new quantitative approach in which the word ‘quantitative’ is used not only to imply calculations and representations with numbers rather than figures but also to indicate that reliability, resolving power, source and extent of errors can be evaluated. These developments have become feasible with advances in computer technology. The present paper deals with some ideas of such a ‘truly quantitative texture analysis’. It compares three inversion methods – conventional harmonic, vector, and WIMV

0021-8898/88/040285-20$03.00

Table 1. *Frequently used symbols*

$\mathbf{y}$	Sample direction.
$\mathbf{h}_i$	Crystal direction.
$f(g)$	Orientation distribution function (ODF).
$f^M(g)$	Method-dependent ODF derived from pole figures.
$\tilde{f}(g)$	Reduced ODF consistent with pole figures (expressed by even harmonic coefficients).
$P_{\mathbf{h}_i}(\mathbf{y})$	Pole figure of crystal direction $\mathbf{h}_i$.
$\mathscr{P}_{\mathbf{h}_i}(\mathbf{y})$	Ideal pole figure, distinguishing positive and negative non-equivalent directions $\mathbf{h}_i$.
$\tilde{P}_{\mathbf{h}_i}(\mathbf{y})$	Centrosymmetric measured ('reduced') pole figure.
$\tilde{P}^M_{\mathbf{h}_i}(\mathbf{y})$	Reduced pole figure recalculated from $f^M(g)$.
$P(\mathbf{h}_i, \mathbf{y})$	Common symbol for various types of pole figures.

– with realistic examples and suggests a uniform approach towards estimation of errors. There are other methods which are not discussed here, including nonlinear iterative harmonic approaches (*e.g.* Bunge, 1987; Liang, Wang & Xu, 1987; Van Houtte, 1983), discrete methods making use of the correction operator concept (*e.g.* Imhof, 1977; Pawlik, 1986; Pospiech, 1987), and ghost correction assuming Gauss functions (*e.g.* Lücke, Pospiech, Jura & Hirsch, 1986). By making the test examples available for distribution we encourage proponents of other methods to use them and compare results with those reported here. Before demonstrating data, it is necessary to review some of the fundamental concepts which are the basis for quantitative texture analysis. We use a general approach which is also applicable to low-symmetry materials which are becoming increasingly important in engineering and geological sciences. Some of the most frequently used symbols are summarized in Table 1.

2. Analytical description of orientation distributions

The orientation of a crystallite is expressed with respect to external specimen coordinates. The relationship of an unequivocally defined right-handed Cartesian coordinate system placed in the crystal $K^c = K_B$ and a right-handed Cartesian coordinate system placed in the specimen $K^s = K_A$ is given by three numbers (symbol g) which represent three rotations to bring K_A into parallelism with K_B. One choice is the set of Euler angles Ψ, Θ, Φ as defined by Roe (1965) (*cf.* Fig. 2)†

$$g \equiv \{\Psi, \Theta, \Phi\}, [K_A \to K_B],$$

$$\text{'G space'}: 0 \le \Psi, \Phi < 2\pi, 0 \le \Theta \le \pi. \qquad (1)$$

Note that the angles Θ and Ψ are identical with the commonly used spherical coordinates θ (pole distance) and φ (azimuth) which define the axis Z_B with respect to K_A. Formally combining (Θ, Ψ) in a unit vector $\mathbf{r}$ we can introduce the symbol (Matthies, 1979)

$$g = \{\Psi, \Theta, \Phi\} \equiv \{\mathbf{r}, \Phi\}, \mathbf{r} = (\Theta, \Psi). \qquad (2)$$

The ODF $f(g)$ describes the probability density to expect crystallites (of unit volume and of a certain kind) which have the orientation g within dg in a polycrystalline sample. Thus

$$f(g) \ge 0,$$

$$\int_G f(g)\,dg \equiv \int_0^{2\pi} d\Psi \int_0^{\pi} \sin\Theta\, d\Theta \int_0^{2\pi} d\Phi f(\{\Psi, \Theta, \Phi\}) = 8\pi^2. \qquad (3)$$

If the crystal symmetry is higher than triclinic, the aforementioned procedure for fixing K_B has N_B equivalent (physically undistinguishable) solutions leading to the (crystal) symmetry relation of the ODF

$$f(g_{B_j} \cdot g) = f(g), \quad g_{B_j} \in G_B, j = 1, 2, \ldots, N_B. \qquad (4)$$

The symmetry group $G_B \equiv G(\mathscr{G}_B)$ is the rotation part of the point group $\mathscr{G}_B$ which describes the crystal structure (crystal class). There are 11 possible pure rotation groups G_B:C_1-1, C_2-2, D_2-222, C_3-3, D_3-312, C_4-4, D_4-422, C_6-6, D_6-622, T-23, O-432.† The sample may also possess a statistical symmetry, resulting in several equivalent K_A:

$$f(g \cdot g_{A_k}) = f(g), \quad g_{A_k} \in G_A, k = 1, 2, \ldots, N_A. \qquad (5)$$

G_A is also a pure rotation group. Because of (4) and (5), the G space (1) can be subdivided into $N_A N_B$ elementary regions which all contain full information about the orientation distribution of a sample (Pospiech, 1982).

The ODF of a texture sample can be determined directly if we are able to measure the orientation of all the individual crystallites which compose it or a statistical representation thereof. This can be done for some, mainly geological, materials with the universal stage microscope (*e.g.* Wenk & Wilde, 1972), or with electron microscopy (*e.g.* Humphreys, 1983). The procedures are laborious and often not applicable to very fine-grained samples. More often information about the ODF is obtained from pole figures. Such pole figures $P(\mathbf{h}_i, \mathbf{y})$ can be interpreted as two-dimensional projections of the three-dimensional ODF $f(g)$ into the projection direction $\mathbf{h}_i$. In practice, $\mathbf{h}_i$ represents a crystal direction with respect to K_B and $\mathbf{y}$ a sample direction with respect to K_A. In order to analyse the

---

†The angles Ψ, Θ, Φ of Roe (1965) are widely used in the American and British texture literature. In theoretical physics they are correspondingly denoted by α, β, γ (*e.g.* Edmonds, 1957; Varshalovic, Moskalev & Chersonskij, 1975). European texture researchers prefer the convention of Bunge (1969), φ_1, Φ, φ_2. The transformation is straightforward and should not cause any difficulties, $\varphi_1 = \Psi + \pi/2$, $\Phi = \Theta$, $\varphi_2 = \Phi - \pi/2$.

$\phi - \pi/2$

†In this discussion of group theory Schoenflies symbols are more appropriate than International symbols.

information contained in pole figures we have to classify them into three different types.

If $\mathbf{h}_i$ is unambiguously fixed with respect to the crystal coordinate system K_B, then the probability that $\mathbf{h}_i$ is pointing in a certain sample direction $\mathbf{y}$ is given by the so-called 'ideal pole figure' $\mathscr{P}_{\mathbf{h}_i}(\mathbf{y})$, with

$$\mathscr{P}_{\mathbf{h}_i}(\mathbf{y}) = \int_G f(g)\delta(\mathbf{h}_i - g.\mathbf{y})\,\mathrm{d}g/2\pi$$

$$= (1/2\pi)\int_0^{2\pi} f(\{\mathbf{h}_i, \bar{\varphi}\}^{-1}.\{\mathbf{y}, 0\})\mathrm{d}\bar{\varphi},$$

$$\int_Y \mathscr{P}_{\mathbf{h}_i}(\mathbf{y})\,\mathrm{d}\mathbf{y} = 4\pi. \qquad (6)$$

Because of the crystal symmetry $G_B(4)$, N_B equivalent K_B (*i.e.* N_B equivalent $\mathbf{h}_i$) exist for every crystallite leading to the property of (crystal) symmetry of the ideal pole figure,†

$$\mathscr{P}_{g_{B_j}.\mathbf{h}_i}(\mathbf{y}) = \mathscr{P}_{\mathbf{h}_i}(\mathbf{y}),\ g_{B_j} \in G_B,\ j = 1, 2, \ldots N_B. \qquad (7)$$

If an infinite number of such ideal pole figures were available, the ODF could be calculated and the solution would be unambiguous (Matthies, 1979, 1982*a*; Bunge & Esling, 1982).

$$f(g) = (1/4\pi)\int_H f(\mathbf{h}, g)\,\mathrm{d}\mathbf{h},$$

$$f(\mathbf{h}, g) = \mathscr{P}_{\mathbf{h}}(-g^{-1}.\mathbf{h}) + (1/\pi)\int_0^{\pi} \mathrm{d}\theta \cos(\theta/2)$$

$$\times\ \mathrm{d}[R(\cos\theta, \mathbf{h}, g)]/\mathrm{d}\cos\theta,$$

with

$$R(\cos\theta, \mathbf{h}, g) \equiv \int_0^{2\pi} \mathscr{P}_{\mathbf{h}}(\{g^{-1}.\mathbf{h}, 0\}^{-1}.\mathbf{y})\,\mathrm{d}\varphi,\ \mathbf{y} = (\theta, \varphi). \qquad (8)$$

In practice only a limited number of pole figures can be measured (strongly diffracting and well separated diffraction peaks *hkl*) and all measurements contain experimental errors. Both factors lead to ambiguity, but the case is further complicated because it is not even possible to measure a single ideal pole figure by diffraction, except in special directions $\mathbf{h}^*$ for which $\mathscr{P}_{\mathbf{h}^*}(\mathbf{y})$ is identical to pole figures of lower content of information described below. Even if anomalous scattering‡ is used (Bunge & Esling, 1981), $N_b^i \geq N_B^i$ equivalent $\mathbf{h}_i$ following from the full crystal symmetry $\mathscr{G}_B$ are present:

$$\mathbf{h}_i^j = g_{b_j}.\mathbf{h}_i,\ g_{b_j} \in \mathscr{G}_B;\ j = 1, 2, \ldots, N_b. \qquad (9)$$

N_b^i is the number of geometrically distinguishable directions in the set of the $\mathbf{h}_i^j$ for a given $\mathbf{h}_i$. Correspondingly N_B^i is connected with the group G_B [*cf.* (7)]. The $N_b^i - N_B^i$ additional equivalent projection directions possess the same Bragg angle in diffraction, and this superposition of diffraction signals leads to the so-called 'unreduced pole figures'

$$P_{\mathbf{h}_i}(\mathbf{y}) = (1/N_b)\sum_{j=1}^{N_b} \mathscr{P}_{g_{b_j}.\mathbf{h}_i}(\mathbf{y})$$

$$= (1/N_b)\left[N_B \mathscr{P}_{\mathbf{h}_i}(\mathbf{y}) + \sum_{j=N_B+1}^{N_b} \mathscr{P}_{g_{b_j}.\mathbf{h}_i}(\mathbf{y})\right], \qquad (10)$$

with $g_{b_j} = g_{B_j}$ for $j = 1, 2, \ldots, N_B$.

The last sum in (10) expresses an overlap of ideal pole figures and does not provide sufficient information to obtain the ODF from (8). This effect does not appear for structures with $\mathscr{G}_B = G_B$. But in this case populations of left- and right-handed enantiomorphs exist which have two ODFs which are superposed in the experimental pole figures and cannot be separated if their correlation is unknown.

For centrosymmetric crystals or for all regular diffraction experiments (Friedel's law) the $+\mathbf{h}_i$ and $-\mathbf{h}_i$ directions are either equivalent in the sense of (9) and (10) or indistinguishable by the experiment, and we can only obtain 'reduced pole figures'

$$\tilde{P}_{\mathbf{h}_i}(\mathbf{y}) = [P_{\mathbf{h}_i}(\mathbf{y}) + P_{-\mathbf{h}_i}(\mathbf{y})]/2$$

$$= (1/\tilde{N}_b)\sum_{j=1}^{\tilde{N}_b} \mathscr{P}_{\tilde{g}_{b_j}.\mathbf{h}_i}(\mathbf{y}) \qquad (11)$$

with $\tilde{g}_{b_j} \in \tilde{\mathscr{G}}_B = \mathscr{G}_B \times C_i,\ j = 1, 2, \ldots, \tilde{N}_b \geq N_b$. Since $\tilde{N}_b \geq 2N_B > N_B$, there is obviously an absolute loss of information leading in principle to ambiguity if the ODF is calculated from measured pole figures.

3. The central problem of pole-figure inversion

In the following discussion we will in general refer only to centrosymmetric crystals (with $\mathscr{G}_B$ belonging to the 11 Laue groups) which compose the vast majority of materials of interest in texture analysis.† In these cases [with $\tilde{P}_{\mathbf{h}_i}(\mathbf{y}) = P_{\mathbf{h}_i}(\mathbf{y})$], there are several solutions when the ODF $f(g)$ is determined from pole figures which have been measured by diffraction techniques. The structure of these solutions is

$$f^M(g) = \tilde{f}(g) + \tilde{\tilde{f}}^M(g). \qquad (12)$$

$\tilde{f}(g)$, which is consistent with all reduced pole figures $\tilde{P}_{\mathbf{h}_i}(\mathbf{y})$, can be determined by (8), using reduced pole figures instead of ideal pole figures. The 'reduced' ODF $\tilde{f}(g)$ has the form

$$\tilde{f}(g) = f(g)/2 + f_G(g) >< 0, \qquad (13)$$

---

† For all types of pole figures considered in the paper the sample symmetry property $P(\mathbf{h}_i, g_{A_k}.\mathbf{y}) = P(\mathbf{h}_i, \mathbf{y})$ follows due to (5).

‡ Only applicable if crystals are noncentrosymmetric and anomalous-scattering contribution is large enough to be measured by texture goniometry.

† For a more detailed analysis of the situation in the case of noncentrosymmetric crystals see, for example, Matthies & Helming (1982); Matthies (1984); Matthies *et al.* (1987).

with the 'ghost part' $\{g^* = [\omega, \mathbf{n}]$, a rotation about a direction $\mathbf{n}(\theta, \varphi)$ through an angle ω (Matthies, 1979)$\}$

$$f_G(g) = f_\pi(g) + f_\Omega(g),$$

$$f_\pi(g) = \int_0^\pi \sin\theta\, \mathrm{d}\theta \int_0^{2\pi} \mathrm{d}\varphi\, f(g.[\omega = \pi, \theta, \varphi])/8\pi \geq 0,$$

$$f_\Omega(g) = \int_0^\pi \mathrm{d}\omega \int_0^\pi \sin\theta\, \mathrm{d}\theta \int_0^{2\pi} \mathrm{d}\varphi\, \tan^2(\omega/2) \times \{f(g.[\omega = \pi, \theta, \varphi]) - f(g.[\omega, \theta, \varphi])\}/8\pi^2 >< 0. \tag{14}$$

Let $\mathscr{F}(g)$ be an arbitrary function with symmetry properties such as (4) and (5). Exchanging $f(g)$ for $\mathscr{F}(g)$ in (13) and (14), we obtain for $\tilde{\tilde{f}}^M(g)$ the most common form $[\mathscr{F}(g) = \tilde{\mathscr{F}}(g) + \tilde{\tilde{\mathscr{F}}}(g)]$

$$\tilde{\tilde{f}}^M(g) = \tilde{\tilde{\mathscr{F}}}(g) = \mathscr{F}(g) - \tilde{\mathscr{F}}(g) = \mathscr{F}(g)/2 - \mathscr{F}_G(g). \tag{15}$$

If we substitute $\tilde{\tilde{f}}^M(g)$ and $f^M(g)$ for $f(g)$ in (11) and (6) respectively [symbol $\hat{\tilde{P}}(\mathbf{h}_i, \mathbf{y}, g)f(g)$], then the following relations are valid:

$$\hat{\tilde{P}}(\mathbf{h}_i, \mathbf{y}, g)\tilde{\tilde{f}}^M(g) = 0, \tag{16}$$

$$\hat{\tilde{P}}(\mathbf{h}_i, \mathbf{y}, g)f^M(g) = \hat{\tilde{P}}(\mathbf{h}_i, \mathbf{y}, g)\tilde{f}(g) = \tilde{P}_{\mathbf{h}_i}(\mathbf{y}). \tag{17}$$

Note that $\tilde{\tilde{f}}^M(g)$ (15) contains an arbitrary function $\mathscr{F}(g)$ and that the true $\tilde{f}(g)$ part of the ODF $f(g) = \tilde{f}(g) + \tilde{\tilde{f}}(g)$ is, like $\tilde{\tilde{f}}^M(g)$, 'invisible' in $\tilde{P}_{h_i}(y)$, *i.e.* $\tilde{\tilde{f}}(g)$ is only one function of a whole set of possible $\tilde{\tilde{f}}^M(g)$ which follow from all $\mathscr{F}(g)$.

In the harmonic representation (Bunge, 1969), the distinction between $f(g)$ and $\tilde{f}(g)$ is particularly transparent. If one uses the symmetrized harmonic functions

$$Y_{l,\tau}(g_j.\mathbf{r}) = Y_{l,\tau}(\mathbf{r}), \quad g_j \in \mathscr{G}, \quad j = 1, 2, \ldots, N, \quad \tau = 1, 2, \ldots, L(\mathscr{G}, l) \tag{18}$$

(Matthies & Helming, 1982),

$$\begin{gathered} D^l_{\mu,\nu}([g_{B_j}.g.g_{A_k}]^{-1}) = D^l_{\mu,\nu}(g^{-1}), \\ g_{B_j} \in G_B, \quad j = 1, 2, \ldots, N_B,\ \mu = 1, 2, \ldots, L(G_B, l) \\ g_{A_k} \in G_A, \quad j = 1, 2, \ldots, N_A,\ \nu = 1, 2, \ldots, L(G_A, l) \end{gathered} \tag{19}$$

and

$$f(g) = \sum_{l=0}^{\infty} \sum_{\mu,\nu} C_l^{\mu,\nu} D^l_{\mu,\nu}(g^{-1}), \tag{20}$$

the relationships discussed above then take (for all possible crystal symmetries) the exact form [$w = 1$ or 0, $\tilde{G}_B \equiv G(\tilde{\mathscr{G}}_B)$]

$$\begin{bmatrix} \mathscr{P}_{\mathbf{h}_i}(\mathbf{y}) \\ P_{\mathbf{h}_i}(\mathbf{y}) \\ \tilde{P}_{\mathbf{h}_i}(\mathbf{y}) \end{bmatrix} = \sum_{l=0}^{\infty} \frac{4\pi}{2l+1} \sum_{\mu,\nu} C_l^{\mu,\nu} \begin{bmatrix} 1 \\ w(G_B, \mathscr{G}_B, l, \mu) \\ w(G_B, \tilde{\mathscr{G}}_B, l, \mu) \end{bmatrix} \times Y^*_{l,\mu}(\mathbf{h}_i)\, Y_{l,\nu}(\mathbf{h}_i), \tag{21}$$

$$w(G_B, \tilde{\mathscr{G}}_B, l, \mu) = w(G_B, \tilde{G}_B, l, \mu)[1 + (-1)^l]/2, \tag{22}$$

$$\tilde{f}(g) = \sum_{l=0(2)}^{\infty} \sum_{\mu,\nu} C_l^{\mu,\nu} w(G_B, \tilde{G}_B, l, \mu) D^l_{\mu,\nu}(g^{-1}), \tag{23}$$

$$\tilde{\tilde{f}}^M(g) = \sum_{l=1(2)}^{\infty} \sum_{\mu,\nu} C_l^{\mu,\nu} D^l_{\mu,\nu}(g^{-1}) + \sum_{l=0(2)}^{\infty} \sum_{\mu,\nu} C_l^{\mu,\nu}[1 - w(G_B, \tilde{G}_B, l, \mu)] \times D^l_{\mu,\nu}(g^{-1}). \tag{24}$$

Because $L(G_B, l) \geq L(\tilde{G}_B, l) \geq L(\tilde{\mathscr{G}}_B, l)$ certain $w(G_B, \tilde{\mathscr{G}}_B, l, \mu)$ are equal to zero, *i.e.* the corresponding $C_l^{\mu,\nu}$ are not 'seen' by reduced pole figures $\tilde{P}_{\mathbf{h}_i}(\mathbf{y})$, especially all $C_l^{\mu,\nu}$ with odd numbers l [*cf* (22)] (Matthies, 1979).† For centrosymmetric crystals with $G_B = \tilde{G}_B$, $w(G_B, \tilde{G}_B, l, \mu) = 1$ is valid. In this case $\tilde{\tilde{f}}^M(g)$ following from the arbitrary function $\mathscr{F}(g)$ in (15) has the form of the first sum in (24) with any $C_l^{\mu,\nu}$ for odd l.

From the foregoing considerations we can conclude that there are two reasons leading to difficulties when the ODF is calculated from pole figures. The first one is related to the insufficient quantity of experimental data (ideally an infinite number is needed), and the second one to their quality (only 'reduced' pole figures can be measured). This can also be elucidated by the following considerations.

The central problem, $\tilde{P}_{\mathbf{h}_i}(\mathbf{y}) \rightarrow f(g)$, in its integral form (11) and (6), can be simplified by discretization. If we introduce N_G cells in the G space and N_Y cells on the pole figure, we obtain a system of N_P linear equations for N_G unknowns with

$$N_P = \sum_{i=1}^{I} N_{P_i}.$$

I is the number of measured pole figures and N_{P_i} the number of data points of cells considered at $\mathbf{y}_j$ ($j = 1, 2, \ldots, N_{P_i}$) in the ith pole figure. For $N_G > N_P$ the problem is undetermined, which can formally be corrected by increasing the volume of G-space cells and thereby decreasing the number of the unknowns N_G. This obviously lowers the resolution. In principle, the condition $N_G \leq N_P$ can be satisfied for a small number I, but a sufficiently large N_{P_i}. But from the structure of the solution (8), I obviously influences the resolution, and it is desirable to use as many pole figures as possible. In addition to the necessary condition $N_G \leq N_P$, there is also a condition of sufficiency of information. That is, even for $N_G \leq N_P$ (neglecting the question of incompatibility of the equations following from the artificial discretization of the problem and from experimental errors) the system of equations may not be sufficient to give an unambiguous solu-

---

†An 'invisibility' of certain $C_l^{\mu,\nu}$ can also rise in (21) for special projection directions $\mathbf{h}_i^*$ owing to $Y_{l,\mu}(\mathbf{h}_i^*) \equiv 0$. For examples see the end of § 7.1.

tion. The criterion for sufficiency is that the rank of the corresponding matrix must be equal to N_G.

As was qualitatively shown by Schaeben (1984), the loss of information about the ODF in reduced pole figures leads to the fact that this rank will always be lower than or equal to $N_G/2$, demonstrating again the 'invisibility' of any $\tilde{\tilde{f}}^M(g)$.

In addition to the distortions due to $\tilde{f}(g) \neq f(g)$ [*cf* (13)], a given $\tilde{\tilde{f}}^M(g)$ can also create maxima and minima, or subsidiary topography changes in $f^M(g)$ [*cf* (12)] which are not present in the true ODF $f(g)$. All these deviations from $f(g)$ have been named 'ghost effects' (Matthies, 1979) and in general depend on the reproduction method used.

The demand for positivity of the solution $f^M(g) \geq 0$ reduces the variation width of possible solutions, at least for strong textures. For instance, if pole figures contain zeros, $\tilde{P}_{\mathbf{h}_i}(\mathbf{y}_m^0) = 0$ at $\mathbf{y}_m^0$, zero regions are created in G space (Bunge & Esling, 1979), reducing the number of the N_G unknowns to N'_G. Indeed, from $f(g) \geq 0$ and the projective character of the pole figures, $f(g_{F_m}) = 0$ (an exact solution!) follows for all points in the G space belonging to the zero fibre [*cf.* (6) and (11)],

$$g_{F_m} \in \{\tilde{g}_{b_j} \cdot \mathbf{h}_i,\ \varphi\}^{-1} \cdot \{g_{A_k} \cdot \mathbf{y}_m^0,\ 0\}$$
$$\tilde{g}_{b_j} \in \tilde{\mathcal{G}}_B,\quad g_{A_k} \in G_A,\quad 0 \leq \varphi < 2\pi. \qquad (25)$$

If there is a sufficient number of pole-figure zeros, the variation width of $f^M(g)$ may disappear. In the discretization approach such a situation arises for $N'_G \leq N_G/2$, *i.e.* if the condition of sufficiency of information is obeyed. Unfortunately the existence of pole-figure zeros depends on the given sample. A subjective definition of the zeros is rather arbitrary and leads only to good ODF approximations for very sharp textures (Lee, Bunge & Esling, 1986).

In the general case of smooth textures, more rigorous assumptions need to be applied to obtain a unique solution. These assumptions may take into account practical experience about the general structure of ODF's following from theoretical models such as that of Taylor (1938) which explains the development of deformation textures. One assumption may be that the ghost-corrected ODF should be as smooth as possible without subsidiary maxima and minima.

Independently of how a ghost-corrected $f^M(g)$ is found, there is a set of demands that needs to be satisfied. The first is that $f^M(g)$ has best to explain the experimental pole figures. Indeed, any $f^M(g)$ (with or without ghosts) explaining the $\tilde{P}_{\mathbf{h}_i}(\mathbf{y})$ better than an $f^{M'}(g)$ derived from the same starting values $\tilde{P}_{\mathbf{h}_i}(\mathbf{y}_j)$ by another method (even with elements of ghost correction) is to be preferred.

The second demand is that because $f(g) \geq 0$, $f^M(g_{F_m}) = 0$ should be exactly [or to a good approximation, *i.e.* $|f^M(g_{F_m})| \ll 1$] realized for the zero fibre (25) belonging to a pole-figure zero $\tilde{P}_{\mathbf{h}_i}(\mathbf{y}_m^0) = 0$.

The third demand is that for any concept of ghost correction the specific properties of the resulting $f^M(g)$ have to be explicitly characterized.

4. Consistency of reproduction methods and quality of experimental data

Although quantitative ODF's have been calculated from pole figures for over 20 years, there is still no generally accepted method for evaluating the difference between experimental and recalculated pole figures. Moreover, even if such data are calculated they are rarely published, which is unthinkable, for instance, in crystal structure analysis where the scrutiny of the R factor is used to evaluate the quality of measurements and/or of the structural interpretation. Errors are due not only to the reproduction method used but also to errors in the experimental data.

4.1. *Error criteria in texture analysis*

In texture analysis experimental pole figures are the principal information which we possess, and a comparison of $\tilde{P}_{\mathbf{h}_i}(\mathbf{y}_j)$ with the corresponding $\tilde{P}^M_{\mathbf{h}_i}(\mathbf{y}_j) = \tilde{P}(\mathbf{h}_i,\ \mathbf{y}_j,\ g) f^M(g)$ recalculated from the reproduced ODF $f^M(g)$ can give us a numerical criterion for the quality of the solution. The 'difference pole figures'

$$\Delta \tilde{P}_{\mathbf{h}_i}(\mathbf{y}_j) \equiv \tilde{P}_{\mathbf{h}_i}(\mathbf{y}_j) - \tilde{P}^M_{\mathbf{h}_i}(\mathbf{y}_j),\quad j = 1, 2, \ldots, J, \qquad (26)$$

are a possibility for demonstrating graphically regions of systematic deviations.

An integral assessment of the quality can be expressed by mean errors R_w weighted with the area S_j of the pole-figure cell c_j around $\mathbf{y}_j$,

$$S_j = \int_{c_j} \sin\theta \,\mathrm{d}\theta \,\mathrm{d}\varphi, \qquad (27)$$

$$R_w = 100\% \sum_{j=1}^{J} S_j |\Delta \tilde{P}_{\mathbf{h}_i}(\mathbf{y}_j)| \Big/ \sum_{j=1}^{J} S_j \tilde{P}_{\mathbf{h}_i}(\mathbf{y}_j). \qquad (28)$$

Alternatively, squared errors can be used to emphasize large deviations. But while such mean errors can indicate problems in data or methods for common physical problems, they may not be most suitable for textures.

Owing to the normalization of the ODF (3), of the pole figures (6), and because of their probability character, the number 1 (random orientation distribution) plays a similar role in texture analysis to the zero for common physical quantities (the boundary between negative and positive values). Indeed, for the textureless case, $f(g) = 1$, $\tilde{P}_{\mathbf{h}_i}(\mathbf{y}) = 1$ is valid, and a value $f(g) > 1$ [$\tilde{P}_{\mathbf{h}_i}(\mathbf{y}) > 1$] can only arise if points with $f(g) < 1$ [$\tilde{P}_{\mathbf{h}_i}(\mathbf{y}) < 1$] exist simultaneously in the G and Y space respectively. In other words, the 'two worlds' $1 < f(g) < \infty$ and $0 \leq f(g) \leq 1$ are to be reproduced with the same accuracy.[†] In this connection the isotropic background ['phon', the Russian word for 'murmur' or 'noise', introduced by Matthies (1984), Matthies & Vinel (1982)] plays an important role.

$$F \equiv \min\{f(g)\}, \quad 0 \leq F \leq 1 \tag{29}$$

can also be interpreted in terms of how many crystallites are 'textured' [100% $(1-F)$] and how many are randomly oriented (100% F).

Analysing error characteristics (28) from this point of view we see immediately that the corresponding expressions discriminate against regions with small values of $\tilde{P}_{\mathbf{h}_i}(\mathbf{y})$ and in diffraction experiments those are most likely to be afflicted with large absolute errors. This inadequacy can be overcome by considering relative deviations such as

$$\mathbf{r}_{ij} = |\tilde{P}_{\mathbf{h}_i}(\mathbf{y}_j) - \tilde{P}^M_{\mathbf{h}_i}(\mathbf{y}_j)| / \tilde{P}_{\mathbf{h}_i}(\mathbf{y}_j).$$

If we introduce a selecting function

$$\Theta(\varepsilon, x) = \begin{cases} 0 \\ 1 \end{cases} \text{for} \begin{cases} x \leq \varepsilon \\ x > \varepsilon \end{cases} \tag{30}$$

the so-called 'RP values' are defined as

$$RP_{i,j}(\varepsilon) \equiv RP_{ij} = 100\% \, \Theta[\varepsilon, \tilde{P}_{\mathbf{h}_i}(\mathbf{y}_j)] \mathbf{r}_{i,j} \tag{31}$$

('local errors') with their special forms

$$\mathrm{RP0}_{i,j} = \mathrm{RP}_{i,j}(0), \quad \mathrm{RP1}_{i,j} \equiv \mathrm{RP}_{i,j}(1), \tag{32}$$

and the corresponding mean quantities RP_i, $\mathrm{RP0}_i$, $\mathrm{RP1}_i$, RP, RP0, and RP1 defined as

$$\mathrm{RP}_i = \sum_{j=1}^{J} \mathrm{RP}_{i,j} \Big/ \sum_{j=1}^{J} \Theta[\varepsilon, \tilde{P}_{\mathbf{h}_i}(\mathbf{y}_j)],$$

$$\mathrm{RP} = \sum_{i=1}^{I} \mathrm{RP}_i / I. \tag{33}$$

The introduction of an $\varepsilon > 0$ permits on the one hand (*e.g.* $\varepsilon = 0{\cdot}005$; this value has been used for all RP0 calculations) the discrimination of meaningless errors arising, for example, from computer inaccuracy. On the other hand (*e.g.* $\varepsilon = 2, 3, 4$), it is possible to explore the quality of reproduction for the main peaks in the pole figures. Notice that RP values are much more sensitive than R_w values and can reach large values (*e.g.* poor statistics, sharp textures measured with bad resolution, series-termination effects, large cells in G space). Whenever RP values are high, difference pole figures should be determined and carefully analysed. RP values could also be weighted as in (27) and (28).

4.2. *Compatibility of pole-figure data*

According to (11) and (6), different pole figures are projections of the same function $f(g)$ and therefore there are certain correlations of pole-figure values within a single pole figure and between different pole figures. Only if these correlations are satisfied and the values are compatible can we expect to find a function which explains the measured data.

Compatibility problems are expressed in quantities such as $\Delta \tilde{P}_{\mathbf{h}_i}(\mathbf{y}_j)$ (26), RP_{ij} (31), or RP_i (33), but this requires that a solution for the ODF has been obtained and a poor agreement can always be attributed to problems with the reproduction method. Therefore it is desirable to evaluate somehow the quality of measurements before a complete ODF reproduction is attempted.

The *external* compatibility between various pole figures can be evaluated by using invariants from group-theoretical considerations (Matthies, 1986). For the F coefficients of the harmonic method (*cf.* § 6.1),

$$F_l^{\nu}(\mathbf{h}_i) = \int_Y \tilde{P}_{\mathbf{h}_i}(y) Y^*_{l,\nu}(\mathbf{y}) \, \mathrm{d}\mathbf{y}, \tag{34}$$

we find for cubic symmetry ($G_B = O$) for $l = l^* \equiv 4, 6, 8, 10, 14$ and a fixed ν and ν' that the ratio [*cf.* (20), $L(O, l^*) = 1$]

$$F_l^{\nu}(\mathbf{h}_i) / F_l^{\nu'}(\mathbf{h}_i) = C_l^{1,\nu} / C_l^{1,\nu'} = K(l, \nu, \nu') \tag{35}$$

is independent of $\mathbf{h}_i$, *i.e.* it has the same value for different pole figures which can be tested.

The *initial* compatibility within a pole figure can be addressed with the 'single pole-figure fit'. A set of data $\tilde{P}_{\mathbf{h}_i}(\mathbf{y}_j)$ can only be called a pole figure if at least *one* function $f_i(g) \geq 0$ exists which has $\tilde{P}_{\mathbf{h}_i}(\mathbf{y})$ as a projection. In this case it is irrelevant whether $f_i(g)$ is compatible with other pole figures or whether it resembles the true ODF $f(g)$. If we calculate $\tilde{P}^M_{\mathbf{h}_i}(\mathbf{y})$ for $f^M(g) = f_i(g)$ and the RP_i value from (33), then RP_i for a single pole-figure fit should always be smaller than the corresponding RP_i for an I pole-figure fit. If RP_i for a single pole-figure fit is bad, it indicates poor internal compatibility.

Single pole-figure fits can be obtained with reproduction methods which contain nonlinear operations (*cf.* §§ 6.2, 6.3). However, the use of single pole-figure fits to evaluate internal compatibility does not imply that we recommend obtaining $f^M(g)$ from a single pole figure. On the other hand, poor pole figures with large internal errors add uncertainty and are better omitted from the analysis. The approximation of $f^M(g)$ by $f_i^M(g)$ is only possible for large regions of zero or uniform background (*cf.* § 3 – the case $N'_G < N_G/2$).

5. Recommendation for a standard procedure

It would be highly desirable if some standard procedure were followed to facilitate comparisons and

---

[†] Note that in common physics the measure of order in systems is connected with the entropy S. For our problem such an entropy will be proportional to $\ln[f(g)]$, with $\ln(1) = 0$ and the two equivalent S regions: $-\infty < S \leq 0$, $0 \leq S < \infty$.

interpretations. We suggest here some quantitative approaches and hope to stimulate discussion on how to implement a more uniform approach. This is particularly important at this time as reproduction methods are increasingly applied to non-cubic materials and to low sample symmetries, particularly in earth sciences. If everyone develops his own system of notations or follows his own conventions in evaluating the quality of his results, there is bound to be chaos (see also in this context the discussions of a panel at the International Conference on Texture of Materials in Sante Fe (Wenk, Bunge, Kallend, Lücke, Matthies, Pospiech & Van Houtte, 1987).

5.1. *Choice of coordinate systems*

5.1.1. *Crystal coordinate system.* The values of the Euler angles which specify the orientation g of a crystallite with respect to sample coordinates K_A depend on how the crystal coordinate system K_B is fixed in the crystal lattice. In the cubic case ($G_B = O$-432), $\mathbf{X}_B$, $\mathbf{Y}_B$, $\mathbf{Z}_B$ are naturally parallel to the orthogonal edges of the unit cell and the same seems appropriate for all other cases with orthogonal edges. For lower crystal symmetry there are several subjective choices.

Matthies *et al.* (1987) propose a uniform system for fixing K_B in the crystal lattice which applies to all 230 space groups. Each space group belongs to one of seven crystal systems which define a unit cell with three basis vectors $\mathbf{A}_1 = \mathbf{a}$, $\mathbf{A}_2 = \mathbf{b}$, $\mathbf{A}_3 = \mathbf{c}$ [see *International Tables for Crystallography,* Vol. A. (Hahn, 1983)]. The monoclinic system is traditionally described in the first setting and hexagonal coordinates are used for the rhombohedral system. Following the rules of Haussühl (1983) we use the right-handed set $\{\mathbf{A}_1, \mathbf{A}_2, \mathbf{A}_3\}$ with

$$(\mathbf{A}_1 . [\mathbf{A}_2 \times \mathbf{A}_3] > 0 \qquad (36)$$

to construct a right-handed Cartesian coordinate system $K(\mathbf{X}, \mathbf{Y}, \mathbf{Z})$:

$$\mathbf{Z} \parallel \mathbf{A}_3, \quad \mathbf{Y} \parallel \mathbf{A}_3 \times \mathbf{A}_1, \quad \mathbf{X} \parallel \mathbf{Y} \times \mathbf{Z}. \qquad (37)$$

This corresponds to the standard convention in crystallography and physics (*e.g.* Nye, 1957). Since the signs of $\mathbf{A}_i$ are not determined and also because lengths a, b, c can be identical due to symmetry, there can be several equivalent possibilities.

Each crystal structure also belongs to a crystal class $\mathscr{G}_B$ with rotation group G_B (Matthies & Helming, 1982). Rules (36) and (37) yield N_B equivalent crystal coordinate systems $\mathbf{K}_B$ for G_B with highest symmetry such as in the hexagonal case $G_B^{\max} = D_6$-622, $N_B^{\max} = 12$. But also included in the hexagonal system are structures with $\mathscr{G}_B = D_{3h}$-$\bar{6}m2$, *i.e.* $G_B = D_3$-312, $N_B = 6$. Among the 12 possible choices there are two physically distinguishable subsets of six. In order to select one of the subsets, positive axis directions can be assigned based on structural details. For the trigonal example ($\mathscr{G}_B = D_{3d}$-$\bar{3}1m$, $G_B = D_3$-312) discussed in § 7, the rhombohedral basis vectors $\mathbf{A}_1$, $\mathbf{A}_2$, $\mathbf{A}_3$ are transformed to hexagonal vectors by $\mathbf{A}'_1 = \mathbf{A}_1 - \mathbf{A}_2$, $\mathbf{A}'_2 = \mathbf{A}_2 - \mathbf{A}_3$ and $\mathbf{A}'_3 = \mathbf{A}_1 + \mathbf{A}_2 + \mathbf{A}_3$, and $\mathbf{Z}_B \parallel \mathbf{A}'_3$, $\mathbf{X}_B \parallel \mathbf{A}'_1$ is chosen.

With such a scheme we can divide the 32 crystal classes into a cubic and hexagonal branch with $G_B^{\max} = O$-432 and $G_B^{\max} = D_6$-622 respectively using the K_B variants of the last ones as starting sets. Then the Euler angles which describe a symmetry element g_{B_j} contained in a given G_B are identical to those of g_{B_j} in $G_B^{\max}$. In order to find equivalent orientations $g^{jk} = g_{B_j} \cdot g \cdot g_{A_K}$ for a given G_B, one has only to consider those g_{B_j} in g^{ik} tables for $G_B^{\max} = O$-432 (Matthies & Wagner, 1981), or $G_B^{\max} = D_6$-622 (Helming & Matthies, 1984), which are contained in G_B.

5.1.2. *Sample coordinate system.* The definition of sample coordinates K_A is more arbitrary. If the sample possesses a statistical symmetry, it is useful to choose axes for K_A which are parallel to symmetry axes such as in rolling of metals with three perpendicular twofold axes. Traditionally, $\mathbf{X}_A$ is chosen parallel to the rolling, $\mathbf{Y}_A$ parallel to the transverse, and $\mathbf{Z}_A$ parallel to the normal direction. In axisymmetric textures $\mathbf{Z}_A$ is parallel to the rotation axis. In torsion experiments it is sensible to place the twofold axis parallel to $\mathbf{Z}_A$ (shear-plane normal parallel to $\mathbf{Y}_A$).

In geological samples symmetry is often lower owing to a complicated strain path. Here it has become customary to use mesoscopic fabric coordinates to define K_A with $\mathbf{Y}_A$ parallel to the lineation and $\mathbf{X}_A$ parallel to the foliation (schistosity) normal. Since rocks are often deformed in plane strain geometry, $\mathbf{Z}_A$ becomes the direction of no deformation. This also makes it easiest to distinguish between pure and simple shear.

It is possible to transform $f(g)$ and define new K_A coordinates after the ODF reproduction has been done (*e.g.* Bunge & Esling, 1985), but this requires considerable effort and it is certainly advantageous to choose K_A before pole figures are measured or to transfer the pole-figure data to the new K_A.

5.2. *Choice of Euler angles*

Euler angles have almost uniformly been accepted as the most efficient method of texture representation. Since the convention of Roe (1965) $g = \{\Psi, \Theta, \Phi\} \mathrel{\hat{=}} \{\alpha, \beta, \gamma\}$ is easier to visualize, particularly for low crystal symmetry, and consistent with crystallographic conventions, we prefer it, but the transformation to the convention of Bunge (1969) is easy (see footnote in § 2) and can be done in final output data without requiring any changes in the computer codes. Another convention which is more symmetrical has been introduced recently by Kocks (1987).

5.3. *ODF representation*

Because of symmetry [(4) and (5)], the G space (1) can be divided into $N_A N_B$ elementary regions, each containing the complete information about the ODF. Usually the ODF is represented within such an elementary region (or a somewhat enlarged region) as a set of planar sections in which densities are contoured. Sections are at constant Φ (or Ψ), and rectangular axes are used for Ψ (or Φ) and Θ as shown in Fig. 1. Unfortunately in such a representation G space and its symmetry are badly distorted, particularly at $\Theta = 0$ or π. In addition, symmetrically related 'texture components' (maxima on ODF) are not very obvious on these maps.

In order to overcome these difficulties a 'spherical' representation was proposed by Wenk, O'Brien & You (1985) and Wenk & Kocks (1987) which is in closer correspondence with pole figures. From (2), the distribution $f(\{\mathbf{r}, \Phi = \text{constant}\})$ can be interpreted as a distribution of $\mathbf{Z}_B$ axes on the surface of a unit sphere and represented as constant Φ sections with Θ and Ψ as spherical coordinates (Fig. 1*b*). The spherical distribution is then represented in equal-area projection which has the added advantage of having an undistorted total texture intensity contained in an orientation peak. Because the angle Φ is known for each section, the full orientation of a component can be immediately constructed using Fig. 2 (Schmidt net). Recently variations to this representation have been proposed (*e.g.* Bunge 1987; Helming, Matthies & Vinel, 1987).

Depending on a particular application, both rectangular and polar representations will no doubt be used. However, we advocate some uniformity in choosing a particular region of G space. Unless the texture displays axial symmetry, we prefer $\Phi = \text{constant}$ sections [called by Wenk & Kocks (1987) COD's or crystal orientation distributions] because the crystal has a strict symmetry which can be rigorously applied, whereas the sample has only a statistical symmetry which is more or less approximated and best seen in $\Phi = \text{constant}$ sections. Of the various equivalent choices for the G-space region (using K_B discussed in § 5.1) we recommend those indicated in Table 2. Because of the inclined position of the threefold axes in the cubic system, elementary regions have a complicated structure (Pospiech, 1982), and it has become customary to represent a threefold enlarged elementary region.

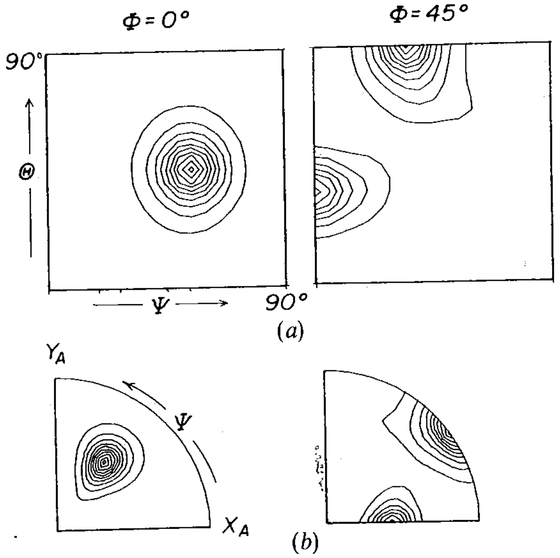

(*a*)

(*b*)

Fig. 1. Comparison of $\Phi = 0$ and $\Phi = 45°$ ODF sections in rectangular (*a*) and spherical (*b*) representations. The example corresponds to $f(g)$ for MIX2 shown in Fig. 4. Lowest contour is 1 m.r.d., contour interval 0·5 m.r.d. (m.r.d. = multiples of a random distribution).

5.4. *Error criteria*

As was explained in § 4, difference pole figures and RP values are informative quantities to assess the quality of experimental data and of the reproduction method and we will discuss them in some detail in § 7. It should become a prerequisite to publish error value for every ODF. Note that experimental pole figures need to be normalized in order to reproduce an ODF and to calculate the error quantities. This leads to additional complications if only incomplete pole figures have been measured.

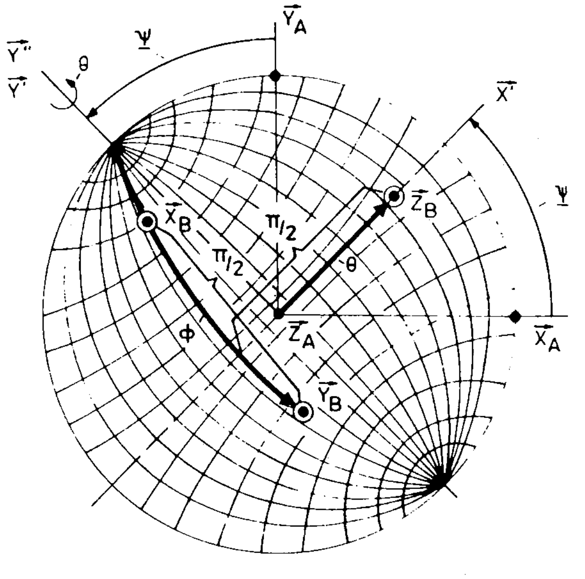

Fig. 2. Definition of Euler angles Ψ, Θ, Φ relating a Cartesian coordinate system placed in the crystal, $K_B(X_B, Y_B, Z_B)$, with a Cartesian coordinate system placed in the specimen, $K_A(X_A, Y_A, Z_A)$. Polar coordinates, equal-area projection. K_A will be parallel to K_B after the three rotations: rotation of K_A around the axis Z_A through the angle $\Psi[K_A \rightarrow K'(X', Y', Z' = Z_A)]$; rotation of K' around the axis Y' through the angle $\Theta[K' \rightarrow K''(X'', Y'' = Y', Z'' = Z_B)]$; rotation of K'' around the axis Z'' through the angle $\Phi[K'' \rightarrow K_B(X_B, Y_B, Z_B)]$.

Table 2. *Recommended G-space region for different sample and crystal symmetries*

Sample symmetry:		
$G_A = C_1$-1	$0 \leq \Psi \leq 2\pi$	
C_2-2	$0 \leq \Psi \leq \pi$	
D_2-222	$0 \leq \Psi \leq \pi/2$	
Crystal symmetry:		
cubic branch		
$G_B = O$-432	$0 \leq \Theta \leq \pi/2$; $0 \leq \Phi \leq \pi/2$	(threefold region)
T-23	$0 \leq \Theta \leq \pi/2$; $0 \leq \Phi \leq \pi$	(threefold region)
D_4-422	$0 \leq \Theta \leq \pi/2$; $0 \leq \Phi \leq \pi/2$	
C_4-4	$0 \leq \Theta \leq \pi$; $0 \leq \Phi \leq \pi/2$	
D_2-222	$0 \leq \Theta \leq \pi/2$; $0 \leq \Phi \leq \pi$	
C_2-2	$0 \leq \Theta \leq \pi$; $0 \leq \Phi \leq \pi$	
C_1-1	$0 \leq \Theta \leq \pi$; $0 \leq \Phi \leq 2\pi$	
hexagonal branch		
$G_B = D_6$-622	$0 \leq \Theta \leq \pi/2$; $0 \leq \Phi \leq \pi/3$	
C_6-6	$0 \leq \Theta \leq \pi$; $0 \leq \Phi \leq \pi/3$	
D_3-312	$0 \leq \Theta \leq \pi/2$; $0 \leq \Phi \leq 2\pi/3$	
C_3-3	$0 \leq \Theta \leq \pi$; $0 \leq \Phi \leq 2\pi/3$	

5.5. *Characteristics of the ghost correction*

The condition $f^M(g) \geq 0$ leads to a nonlinear problem that can only be solved in an iterative way. The starting estimate of the ODF solution, the iteration algorithm (which may contain hidden conditions) and explicitly formulated additional conditions all determine the resulting $f^M(g)$. Its properties should be clearly specified. One of the parameters which characterizes $f^M(g)$ is, for example, the texture index (sharpness of the ODF)

$$f^2 \equiv \int_G f^2(g)\, \mathrm{d}g/8\pi^2 \simeq \sum_{n=1}^{N_G} f_n^2 V_n/8\pi^2 \tag{38}$$

with V_n the volume of the nth G-space cell.

6. Some features of reproduction methods

Some aspects of the approach recommended above will be applied in § 7 to realistic examples. Three methods of quantitative texture analysis will be compared using the same input data, the same computer facilities, and presently existing programs which have been tested by those who developed them. A brief discussion of the algorithms used in these three methods and of their characteristic properties seems appropriate [see also Matthies (1984), Wenk (1985) and Wenk, Bunge, Kallend, Lücke, Matthies, Pospiech & Van Houtte (1987) for more details and other methods].

6.1. *Harmonic method*

In the 'conventional harmonic method' (Bunge, 1969, 1982; Bunge & Esling, 1982), Fourier coefficients $C_l^{\mu\nu}$ (20) are obtained through their relationship (21) with experimental values $\tilde{P}_{\mathbf{h}_i}(\mathbf{y}_j)$ $(i = 1, 2, \ldots, I;$ $j = 1, 2, \ldots, J)$. Because of the factor w, it is only possible to obtain $\tilde{f}^L(g) > < 0$ $\left[cf.\ (23)\ \text{with}\ \sum_{l=0(2)}^{L}\right]$ which contains a ghost part (13) and L-dependent termination errors. In general, instead of (21) one uses equations which refer to only one l,

$$F_i^{\nu}(\mathbf{h}_i) = \frac{4\pi}{2l+1} \sum_{\mu=1}^{L(G_B,\, l)} C_l^{\mu,\nu} w(G_B, \tilde{\mathscr{G}}_B, l, \mu)\, Y_{l,\mu}^*(\mathbf{h}_i), \tag{39}$$

or modified equations deduced from them by a least-squares algorithm (Bunge, 1969) [see also (34)].

The solubility of (39) for the unknown $C_l^{\mu,\nu}$ with $w = 1$ depends on the degree of the expansion L and the number of available pole figures $I[L(\mathscr{G}_B, L) \leq I]$. L also determines the resolution in $\tilde{f}^L(g)$ which can be described with the orientation distance $\Delta\omega_L \simeq 2\pi/L$. Let b be the half-width of an ODF peak. In order to obtain a good reproduction, the expansion should extend to a degree L based on a sufficient number of pole figures I (in each the distance in the measuring grid ΔY should be less than $b/2$), such that $\Delta\omega_L < b$. In the harmonic method, errors depend, in addition to data quality, on series-termination effects, computer precision, and the integration algorithm used for (34) (Humbert, 1976).

A rough approximation is obtained by the rectangle method

$$\int_Y \tilde{P}_{\mathbf{h}_i}(\mathbf{y})\, Y_{l,\nu}^*(\mathbf{y})\, \mathrm{d}\mathbf{y} \simeq \sum_{j=1}^{J} \tilde{P}_{\mathbf{h}_i}(\mathbf{y}_j)\, Y_{l,\nu}^*(\mathbf{y}_j) S_j.$$
$$S_j = \int_{Y_j} \mathrm{d}\mathbf{y}. \tag{40}$$

More accurate is the staircase approximation

$$\int_Y \tilde{P}_{\mathbf{h}_i}(\mathbf{y})\, Y_{l,\nu}^*(\mathbf{y})\, \mathrm{d}\mathbf{y} \simeq \sum_{j=1}^{J} \tilde{P}_{\mathbf{h}_i}(\mathbf{y}_j) \int_{Y_j} Y_{l,\nu}^*(\mathbf{y})\, \mathrm{d}\mathbf{y}, \tag{41}$$

which is used in many standard programs. The smallest integration errors are obtained by means of one-dimensional (Dahms & Bunge, 1986) or two-dimensional cubic splines.

The possibilities of the conventional harmonic method are limited by $L(I)$, which is particularly critical for materials with low symmetries where only a few pole figures can be measured satisfactorily. Computer time (for $L \simeq 20$) is low, particularly if functions $D_{\mu,\nu}^l(g_n^{-1})$, $Y_{l,\nu}(\mathbf{y}_j)$ and $Y_{l,\mu}(\mathbf{h}_i)$ are stored in a library. With increasing L the size of these arrays increases rapidly and the large number of terms (positive and negative) in the sums may cause problems with roundoff errors.

The positivity condition $f^M(g) \geq 0$ can be used for a ghost correction such as in the zero domain method (Bunge & Esling, 1979) or in Van Houtte's (1983) $f = h^2$ approach. Both methods are based on $\tilde{f}^L(g)$, constructing $\tilde{\tilde{f}}^M(g)$ such that $\tilde{f}^L(g)+\tilde{\tilde{f}}^M(g)\gtrsim 0$ and that [in accordance with (16) and (17)] the RP value for $f^L(g)$ is not increased (see also Wenk, Bunge, Kallend, Lücke, Matthies, Pospiech & Van Houtte, 1987).

Another approach for a ghost correction, especially useful for interpretations, is to model the ODF with a set of N Gauss functions

$$f^M(g)=F_c+\sum_{n=1}^{N} I_n f(b_n, g_n^0, g)\geq 0, \qquad F_c+\sum_{n=1}^{N} I_n=1. \tag{42}$$

The parameters (intensity I, half-width b and position g^0, isotropic background F_c) are determined by fitting $\tilde{f}^L(g)$ and $\tilde{f}^{ML}(g)$ (Lücke *et al.*, 1986; Matthies, 1982*b*). This method is useful for sharp textures with few components (*e.g.* f.c.c. metals deformed by rolling); medium textures do not as a rule really consist of separate Gauss functions forming complicated distributions, and in this case the method is at best an approximation. Furthermore, $\tilde{f}^M(g)$ (without termination errors) may not be identical with $\tilde{f}^L(g)$. Therefore the RP values for $\tilde{f}^M(g)$ and $\tilde{f}^L(g)$ are generally different. In the examples considered in the following sections we will deal with the conventional harmonic method only.

6.2. *Vector method*

The vector method (Ruer & Baro, 1977; Schaeben, Vadon & Wenk, 1985; Vadon, 1981) discretizes the task $\tilde{P}_{\mathbf{h}_i}(\mathbf{y}_j)\to f(g_n)$ into a set of linear equations which are solved directly with an iterative procedure such that $f(g_n)\geq 0$. The iteration algorithm with a zero approximation $f_0^M(g)=1$ produces a solution $f^V(g)\geq 0$ with a minimal texture index (Matthies, 1984) which is close to $\tilde{f}(g)$. Schaeben's (1984) attempts to suppress secondary minima have not yielded significant improvements because the main properties of the iteration algorithm are maintained. Only in the case of sharp textures with large zero regions in the pole figures will $f^V(g)$ be close to $f(g)$.

The resolution of the vector method depends largely on the size of cells in G and Y space. Since $N_G < IN_Y$ is a necessary condition, the ODF discretization is generally much coarser than the pole-figure grid. The method works with large (but sparse) matrices in the range $N_G N_Y$, which implies a lot of computer time and large storage capacity for low symmetry and also, if good resolution is required, a large number of pole figures.

6.3. *WIMV method*

Based on principles of earlier reproduction methods (Williams, 1968; Imhof, 1982) and on a detailed analysis of the origin of 'ghosts', Matthies & Vinel (1982) developed an iterative reproduction method with a conditional ghost correction which supplies for minimal RP values $f^M(g)\geq 0$ with a maximum texture index (few but sharp peaks) (see also Matthies, 1982*a*; Matthies & Wenk, 1985).

The basic elements of the method are product functions of the type

$$\prod_{i=1}^{I}\prod_{m_i=1}^{M_i}\tilde{P}_{\mathbf{h}_i}(g^{-1}.\mathbf{h}_{m_i}),\quad \mathbf{h}_{m_i}\in\tilde{g}_{b_j}.\mathbf{h}_i,\quad \tilde{g}_{b_i}\in\tilde{\mathscr{G}}_B, \tag{43}$$

whereby $f^M(g)$ is always ≥ 0 and it produces an exact solution for every zero fibre associated with $\tilde{P}_{\mathbf{h}_i}(\mathbf{y}_m^0)=0$ (25), *i.e.* $f(g_{F_m})=0$. These conditions are augmented by requiring a maximum phon $F\equiv\min\{f^M(g)\}\to\max$ for a minimum RP. The method needs neither harmonic functions nor matrix operations, and works with positive numbers only. For its effective organization the method requires rather large arrays of stored addresses defining the cells in G space [*cf.* (6), (11), $g=\{\tilde{g}_{b_j}.\mathbf{h}_i,\ \varphi_n\}^{-1}.\{\mathbf{y}_m,\ 0\}$] or in pole-figure space [*cf.* (43), $\mathbf{y}=g_n^{-1}.\mathbf{h}_{m_i}$] which contain corresponding g or $\mathbf{y}$. The method converges rapidly and permits – as does the vector method – analysis of the internal compatibility of single measured pole figures.

For pole figures with poor statistics it is advisable to smooth $f^M(g)$, for example, by convolution with Gaussians such as for single grain measurements (Wagner, Wenk, Esling & Bunge, 1981) or by filtering. Such filtering of high frequencies which contain no information is effectively achieved in the harmonic method by series termination; however, this does not guarantee that $f^M(g)\geq 0$.

In concluding this short summary of principles it should be emphasized that mathematically correct reproduction methods should produce for the same input pole figures similar RP values (*i.e.* similar recalculated pole figures) except for differences in the degree to which the input information is used. However, depending on the method-specific properties of the result, there are differences in $f^M(g)$.

7. Numerical comparison of methods

The methods described above are all mathematically sound and can reproduce ODF's within the limitations which we have indicated. Whereas ODF's vary because of inherent assumptions, each method should be able to regenerate the original pole figures which served as input within the resolution which depends on discretization, degree of expansion, *etc.* We have used several sets of input pole figures and analysed the same data with the same computer to obtain information about resolution, errors, computer time, memory, and disk storage requirements.† The computer

---

†The pole-figure data for all test examples are available for distribution and may be obtained by sending an IBM PC floppy disk to H.-R. Wenk.

Table 3. *Computer programs*

Method	Specification	Author
Cubic–orthorhombic harmonic (incomplete pole figures)	Rectangular integration	Based on Jura, Pospiech & Bunge (1976)
	Staircase integration	Based on Bechler-Ferry, Wagner, Humbert, Esling & Baro (1981)
Trigonal–triclinic harmonic	Staircase integration	Wagner (1984)
Vector		Vadon (1981), modified by Schaeben (1984)
WIMV		Matthies & Vinel (1982), modified by Matthies & Wenk

used was an IBM 3081 with the VM/SP CMS operating system. Programs used were the most advanced versions at the time, kindly supplied by proponents of each method (Table 3). In each case we tried to get optimum results. Comparisons are done on two levels: experimental and recalculated pole figures (Figs. 3, 5, 7, and 9) and ODF's (Figs. 4, 6, 8, and 10). In three examples (cubic and trigonal standard distributions as well as Taylor simulation) the initial ODF was known and pole figures were generated from the known ODF. In the last example (measured pole figures) the true ODF is unknown. Input pole figures contain normalized densities in a 5 × 5° array with four-digit accuracy. Whereas these data represent densities at θ and φ values of 0, 5° *etc.*, all methods discussed here assume that this value is constant over the size of the box, *i.e.* from 0 to 2·5°, 2·5 to 7·5° *etc.* Output pole figures as well as ODF's were calculated in the same 5° grid. In the case of the vector method some additional comments are in order. First, it uses a different pole-figure grid with boxes extending from 0 to 5°, 5 to 10° *etc.* This clearly has advantages for programming because it avoids special-case situations at borders. Secondly, the vector method uses different coordinates in ODF space (Ruer, 1976). It therefore requires interpolation to bring input and output data into conformity. This was done in such a way as to maintain maxima and minima during the necessary smoothing. It turned out that uncertainties introduced during interpolation are smaller than those inherent in the method. Equal densities in these arrays were then contoured (using a contouring routine designed by Vadon, private communication) and are represented in polar coordinates in equal-area projection. Table 3 describes the computer codes. Table 4 contains information about central processor time; Tables 5–8 contain RP error values and additional information about pole figures and ODF's.

7.1. *Standard distributions*

Properties of each method can best be illustrated if we assume a model ODF $f(g)$ and calculate from it mathematically a set of pole figures $\tilde{P}_{\mathbf{h}_i}(y)$. These pole

Table 4. *Typical computer processor times* (*IBM VP/CMS* 3081 *Level* 0313)

Method		Pole figures	Time (s)	Details
WIMV	cubic	1	4	1 FON step
	cubic	3	7	≤10 iterations
	trigonal	3	28	
	trigonal	6	63	
Harmonic	cubic	3	<2	$L = 16, \tilde{f}$
	trigonal	6	50	
Vector	cubic	1	97	200 iterations
	cubic	3	184	
	trigonal	3	533	

This does not include calculation of data arrays, matrices and library functions and except for WIMV also does not contain the calculation of ODF sections.

figures which serve as input are free of experimental errors. With such an approach not only can we compare pole figures $\tilde{P}_{\mathbf{h}_i}(\mathbf{y}_j) \leftrightarrow \tilde{P}^M_{\mathbf{h}_i}(\mathbf{y}_j)$ but also ODF's $f(g) \leftrightarrow f^M(g)$. We have to guarantee that errors produced in calculating pole figures [(6), (11)] are negligibly small. This can be achieved with so-called standard functions (Matthies, 1980*b*, 1982*b*). Corresponding computer programs were developed at Rossendorf (Matthies *et al.*, 1987) for all $\mathscr{G}_B$ and $G_A = D_\infty, C_\infty, D_2, C_2, C_1$ mixing bell-shaped distributions [*cf.* (42)] of Gaussian or Lorentzian form at g^0_n with any half-width b_n and intensity I_n. With these programs it is possible to calculate $f(g)$, $\tilde{f}(g)$, $\tilde{P}_{\mathbf{h}_i}(\mathbf{y})$, $F^\nu_l(\mathbf{h}_i)$ and $C^{\mu,\nu}_l$ with a 'standard accuracy' (*e.g.* $|\Delta f|$, $|\Delta \tilde{f}|$, $|\Delta P| \leq 0{\cdot}005$).†

*Cubic–orthorhombic symmetry – MIX*2 [*Figs.* 3, 4; *Table* 5; *see also Matthies & Vinel* (1982)]. The standard ODF in Fig. 3(*a*) consists of three components which approximate a f.c.c. rolling texture ($b_1 = b_2 = b_3 = 17°$; isotropic background $F_c = 0{\cdot}3095$).

$$g^0_1 = \{011\}\langle 211\rangle = \{\Psi = 54{\cdot}74,\ \Theta = 45,\ \Phi = 0°\},$$
$$\text{'brass component'},\ I_1 = 0{\cdot}315,\ \text{Lorentzian.}$$

$$g^0_2 = \{123\}\langle 634\rangle = \{\Psi = 31{\cdot}02, \Theta = 36{\cdot}7, \Phi = 26{\cdot}56°\},$$
$$\text{'}S\text{ position'},\ I_2 = 0{\cdot}315,\ \text{Lorentzian.}$$

$$g^0_3 = \{112\}\langle 111\rangle = \{\Psi = 0,\ \Theta = 35{\cdot}26,\ \Psi = 45°\},$$
$$\text{'copper component'},\ I_3 = 0{\cdot}0605,\ \text{Gaussian.}$$

Using the cubic–orthorhombic equivalence $\{\Psi, \Theta, \Phi\} = \{\pi - \Psi, \Theta, \pi/2 - \Phi\}$ (Matthies & Wagner, 1981), we used the threefold elementary G-space region {0–180°, 0–90°, 0–45°} which allows a compact representation. A special property of the MIX2 distribution is the

---

† The difference between these standard functions and the Gaussian distribution suggested by Bunge (1969) consists, among other things, in their analytical closed form for $f(g)$, $\tilde{f}(g)$ and $\mathscr{P}_{\mathbf{h}_i}(\mathbf{y})$. This permits calculation of the corresponding quantities without harmonic series which are unfavorable for high-precision calculations, especially for peaks with small half-widths.

positivity of its reduced part $[\tilde{f}(g) \geq 0{\cdot}06]$ shown in Fig. 4 (Fs). Therefore it is to be expected that the vector method will provide an ODF close to $\tilde{f}(g)$. For a sufficiently large L and a sufficient number of pole figures the harmonic method should also reproduce $\tilde{f}(g)$ with good quality.

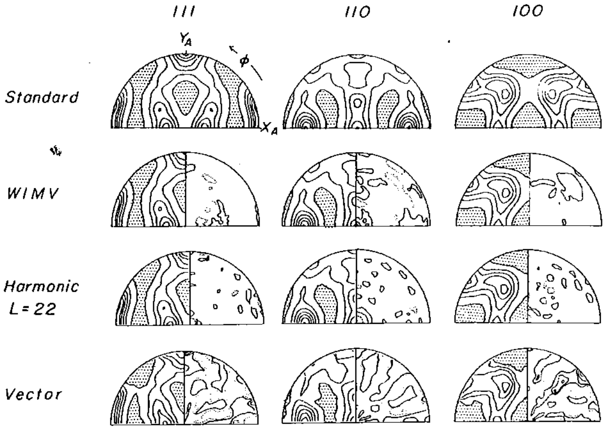

Fig. 3. Cubic–orthorhombic model texture MIX2, consisting of three bell-shaped components described by standard functions. The corresponding standard pole figures $\tilde{P}_{h_i}(\mathbf{y})$ are compared with recalculated pole figures using different reproduction methods (three pole-figure fits). Difference pole figures are shown on the right side. Equal-area projection. Contour intervals for pole figures are 0·25 m.r.d., shaded below 0·75 m.r.d. Contours for difference pole figures are −0·3, −0·2, −0·1, −0·01 (dotted), 0·01, 0·1, 0·2, 0·3 m.r.d. (solid).

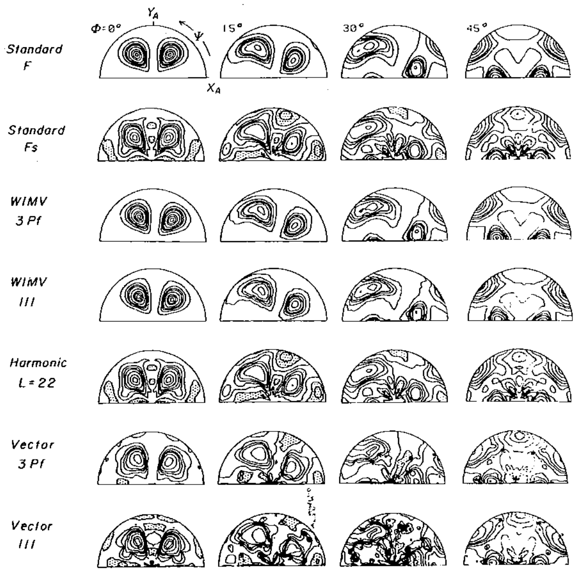

Fig. 4. The ODF of the cubic–orthorhombic model texture MIX2 represented as Φ sections in polar coordinates, equal-area projection. F is model $f(g)$, Fs $=\tilde{f}(g)$, WIMV, Harmonic, Vector are ODF's reproduced with the respective methods. Contours are 0·25, 0·5, 0·75, 1, 1·5, 2, 3, 4, 5 m.r.d. Shaded below 0·5 m.r.d.

Fig. 3 shows contoured 'standard' pole figures 111, 110, and 100 based on a 5° data grid which served as input for the ODF reproduction. They are compared with the recalculated ones. Those from the harmonic method ($L = 22$) and from WIMV are very similar, whereas those from the vector method have peaks at correct positions but of lower intensity, which we attribute to the large cell size in $f(g)$ space.

Interesting information is revealed in difference pole figures (26). For WIMV there is a fairly random scatter of slightly positive and slightly negative areas on all pole figures. The strongest positive deviations ($<0{\cdot}08$ m.r.d.) (m.r.d. = multiples of a random distribution) are close to texture peaks. They often represent single values, suggesting occasional problems due to the simple treatment of the G-space cell structure. Such effects could be eliminated by filtering, as mentioned above.

In the harmonic method the range of errors is similar ($<0{\cdot}04$ m.r.d.), but there is very little correlation with the texture. However, there is a conspicuous minimum in the center of all pole figures which we attribute to the typical poor numerical accuracy of the $C_l^{\mu,\nu=1}$ coefficients.

Deviations are most profound in the vector method. We discern that on the center of each peak located near the equator there is a positive deviation, and this is bordered by a negative area. Deviations show mainly an azimuthal (φ) spread and are simply due to broadened peaks in the recalculated figures. We attribute this to the large cell size and the particular cell pattern in G space which is particularly unfavorable at large Θ.

The ODF's in Fig. 4 illustrate that, as expected, the harmonic method reproduces with good accuracy $\tilde{f}(g)$ with ghost features (Fs). Not only peaks, peak shapes, and peak intensities but also regions with low values of $f^M(g)$ agree closely with $\tilde{f}(g)$. Since the half-width of peaks is $b = 17°$ an expansion to $L = 22$ (*cf.* § 6) is sufficient to resolve the topography. Table 4 illustrates that RP values improve only very slightly for $L > 16$. The WIMV solution is obtained either with $F = P_{\min} = \min\{\tilde{P}_{h_i}(\mathbf{y}_j)\}$ or after three steps in phon iterations beginning with $F_0 = 0$ which yield $f^M_{\min} = 0{\cdot}49$, $0{\cdot}54$, $0{\cdot}55$ respectively after three to six internal iterations. This solution is close to $f(g)$, demonstrating the usefulness of the WIMV conditions for this difficult test (high background, unknown). Of course, for examples with many more than three components of various magnitudes the difference between $f(g)$ and $f^M(g)$ may be larger because WIMV (explaining the pole figures) prefers a solution with a maximum texture index. This explains why peaks in $f^M(g)$ are slightly larger than in $f(g)$. The solution of the vector method in this example with no pole-figure zeros is close to $\tilde{f}(g)$, but resolution is considerably worse than with the harmonic method. For cubic crystal symme-

e figures 111,
ıich served as
ıre compared
the harmonic
very similar,
ıave peaks at
.y, which we
ace.
lifference pole
ıirly random
ıegative areas
ve deviations
ındom distri-
ften represent
·blems due to
.ructure. Such
as mentioned

·rors is similar
rrelation with
ous minimum
ttribute to the
the $C_l^{\mu,\nu=1}$

ector method.
peak located
ıtion, and this
·iations show
simply due to
gures. We at-
particular cell
ınfavorable at

; expected, the
accuracy $\tilde{f}(g)$
;, peak shapes,
ith low values
the half-width
= 22 (*cf.* § 6) is
ɔle 4 illustrates
tly for $L > 16$.
with $F = P_{\min}$
·hon iterations
$_{\text{in}} = 0{\cdot}49$, 0·54,
·nal iterations.
ɔnstrating the
·r this difficult
)f course, for
ɔomponents of
ween $f(g)$ and
explaining the
a maximum
s in $f^M(g)$ are
n of the vector
·figure zeros is
bly worse than
ɔrystal symme-

Table 5. *Error analysis of cubic–orthorhombic standard model* (*MIX*2)

Pole figures	Method*	*I*†	Maximum	Minimum	RP0 (%)	RP1 (%)
111	Model		2·43	0·63		
	W	3	2·43	0·62	0·46	0·55
	W	1	2·38	0·63	0·45	0·55
	*Hr*22	3	2·29	0·62	0·90	0·43
	*Hs*18	3			1·62	1·83
	*Hs*22	3			0·54	0·54
	*Hs*34	3			0·40	0·45
	V	3	2·09	0·59	2·90	2·73
	V	1	2·10	0·64	1·50	1·49
110	Model		2·34	0·68		
	W	3	2·32	0·67	0·86	1·06
	*Hr*22	3	2·31	0·67	0·55	0·57
	*Hs*18	3			1·26	1·56
	*Hs*22	3			0·66	0·86
	*Hs*34	3			0·44	0·56
	V	3	2·19	0·65	2·69	2·55
100	Model		1·91	0·55		
	W	3	1·92	0·55	0·55	0·80
	*Hr*22	3	1·87	0·55	0·78	0·57
	*Hs*18	3			1·11	1·39
	*Hs*22	3			0·55	0·62
	*Hs*34	3			0·31	0·40
	V	3	1·90	0·55	3·89	4·54
ODF	Model f		5·77	0·54		
	Model $\tilde{f}$		4·88	0·06		
	W	3	6·00	0·55	0·63	0·80
	W‡	1	5·89	0·48	0·57	0·68
	*Hr*22	3	4·66	0·04	0·74	0·52
	*Hs*18	3	4·27	0·09	1·33	1·59
	*Hs*22	3	4·62	0·05	0·58	0·67
	*Hs*34	3	4·87	0·06	0·38	0·47
	V	3	4·35	0·03	3·17	3·28
	V	1	5·55	0·01	1·50	1·49

*W = WIMV, V = Vector, H = Harmonic (r = rectangle, s = staircase integration).
†I = number of pole figures used.
‡Without phon iteration.

Table 6. *Error analysis of trigonal–triclinic Gauss standard peak* (*WIMV without phon iteration*)

Pole figures	Method*	*I*	Maximum	Minimum	RP0 (%)	RP1 (%)
006	Gauss		6·82	0·55		
	W	6	6·91	0·54	0·73	1·25
	W	3	6·88	0·54	0·59	1·05
	Hr	6	6·83	0·51	1·29	0·27
	Hs	6	6·76	0·55	0·15	0·36
	V	3	7·16	0·42	10·8	8·5
104	Gauss		2·63	0·55		
	W	6	2·61	0·55	1·28	0·77
	W	3	2·62	0·56	0·93	0·63
	Hr	6	2·63	0·55	1·02	0·37
	Hs	6	2·60	0·56	0·19	0·21
	V	3	2·65	0·44	6·3	4·7
012	Gauss		2·63	0·55		
	W	6	2·61	0·54	1·50	1·44
	W	3	2·60	0·55	1·08	1·12
	Hr	6	2·67	0·55	1·45	2·15
	Hs	6	2·61	0·55	0·24	0·23
	V	3	2·46	0·49	14·9	8·0
202	Gauss		2·64	0·55		
	W	6	2·67	0·54	1·44	1·14
	Hr	6	2·65	0·54	1·02	0·32
	Hs	6	2·62	0·55	0·21	0·21
$2\bar{1}3$	Gauss		1·62	0·55		
	W	6	1·62	0·55	0·90	1·09
	Hr	6	1·63	0·55	0·88	1·04
	Hs	6	1·60	0·55	0·19	0·16
$2\bar{1}0$	Gauss		2·63	0·55		
	W	6	2·62	0·54	0·90	1·00
	Hr	6	2·63	0·54	1·23	0·36
	Hs	6	2·61	0·55	0·20	0·22
ODF	Gauss f		20·03	0·55		
	Gauss $\tilde{f}$		13·19	−0·53		
	W	6	20·31	0·37	1·12	1·11
	W	3	20·32	0·42	0·87	0·93
	*Hr*16	6	13·38	−0·75	1·15	0·75
	*Hs*16	6	13·10	−0·54	0·23	0·23
	V	3	16·8	0·0	10·7	7·1

*Symbols as for Table 5.

try an ODF can be obtained from a single (111) pole figure (Vadon, 1981) and in the MIX2 case with a large isotropic background which reduces the number of unknowns, the single pole-figure fit is very good, particularly with WIMV. With the harmonic method a single pole-figure fit provides unsatisfactory resolution ($L = 10$), and application of nonlinear algorithms is extremely cumbersome. Compared with the other two methods, the vector method produces less-accurate results with a more substantial computational effort.

Trigonal–triclinic Gauss (*Figs.* 5 *and* 6 *and Table* 6). A second example is that of a single Gauss peak ODF for trigonal crystal ($\bar{3}$ $2/m$) and triclinic specimen symmetry. Such textures are common for phyllosilicates in many rocks (Oertel, 1985). We use the example mainly to illustrate the geometry of an orientation represented as pole figures and an ODF for a low-symmetry case. The Gauss component is at $g = \{120°, 60°, 105°\}$ with $b = 36°$, $I = 0{\cdot}45$. An isotropic background $F_c = 0{\cdot}55$ is added. In this example the positive $\mathbf{X}_B$ axis points in the $[2\bar{1}.0]$ direction (hexagonal indexing) and $c/a = 3{\cdot}419$ as in the case for the mineral calcite. Whereas $f(g)$ is fairly monotonic, $\tilde{f}(g)$ displays a more complex pattern, with subsidiary peaks (ghosts) and negative areas.

With six available pole figures the conventional harmonic method is limited to $L = 16$, which is sufficient for a peak width $b = 36°$. Distributions for $\tilde{f}^M(g)$ and $\tilde{f}(g)$ are very similar, including maxima (13·4 *versus* 13·2) and minima ($-0{\cdot}75$ *versus* $-0{\cdot}53$). Differences between $\tilde{P}^M_{\mathbf{h}_i}(\mathbf{y})$ and $\tilde{P}_{\mathbf{h}_i}(\mathbf{y})$ are thought to be due to integration errors, roundoff errors (single precision, real × 4 = 6 digits) and cell size.

In the vector method the computer environment is prohibitive for treatment of more than three triclinic pole figures. In the trigonal case, G cells are large (Δg up to 30°), which limits resolution and effectively reduces peak intensities. Concentrations appear close to the correct positions but are weaker throughout. Conversely, the background is higher. The solution $f^M(g)$ is close, because of the large region with a flat plateau, in general pattern and peak maximum to $f(g)$. Error values are much worse than for the harmonic analysis, but ghosts are largely absent and there are no negative areas.

The WIMV analysis for both three and six pole figures reproduces $f(g)$ with excellent accuracy, but the WIMV conditions are admittedly ideally tailored to such a simple model distribution. Note that the maximum for WIMV is slightly larger than in $f(g)$ (20·3 *versus* 20·0) and much larger than the maximum in $\tilde{f}(g)$ (13·2). In Fig. 5 we also show a recalculated ideal pole figure $\mathscr{P}_{\mathbf{h}_i}(\mathbf{y})$ for $\mathbf{h}_i = \langle 2\bar{1}.0\rangle \parallel +\mathbf{X}_B$ [*cf.* (6)].

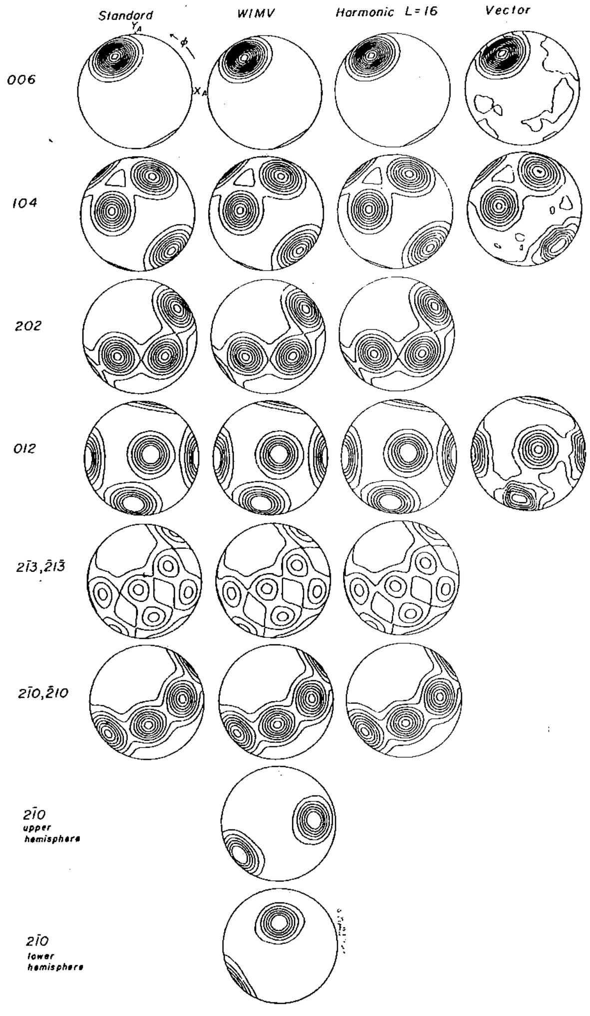

Fig. 5. Trigonal–triclinic Gauss at $\Psi = 120$, $\Theta = 60$, $\Phi = 105°$. Standard pole figures $\tilde{P}_{\mathbf{h}_i}(\mathbf{y})$ are compared with recalculated pole figures using different reproduction methods. The ideal pole figure $+\langle 2\bar{1}.0\rangle$ $\mathscr{P}_{\mathbf{h}_i}(\mathbf{y})$ is also shown on upper and lower hemispheres. Equal area projection, contour interval for 006 is 2 m.r.d., for all others 1 m.r.d., lowest contour is 1·0 m.r.d.

In the case of trigonal $\bar{3}\ 2/m$ symmetry, positive and negative directions $[uv.w]$ which are not perpendicular to a twofold rotation axis are physically different and can be distinguished (Weiss & Wenk, 1985). $\langle 2\bar{1}.0\rangle$ is such an example. $\langle 2\bar{1}.3\rangle$ is another but is not shown. For all other pole figures $\langle 00.6\rangle$, $\langle 10.4\rangle$, $\langle 20.2\rangle$, and $\langle 01.2\rangle$, $\mathbf{h}_i^*$ and $-\mathbf{h}_i^*$ are related by a twofold rotation and are therefore indistinguishable, even in correlation to other crystal directions. In these cases $\mathscr{P}_{\mathbf{h}_i^*}(\mathbf{y}) = P_{\mathbf{h}_i^*}(\mathbf{y}) = \tilde{P}_{\mathbf{h}_i^*}(\mathbf{y})$ and correspondingly information is lost. In the WIMV analysis the initial phon was set to zero. Already after the first refinement cycle $f^M_{\min}$ converged close to $f_{\min}$. A second phon iteration (using $f^M_{\min}$ as starting value) improved the

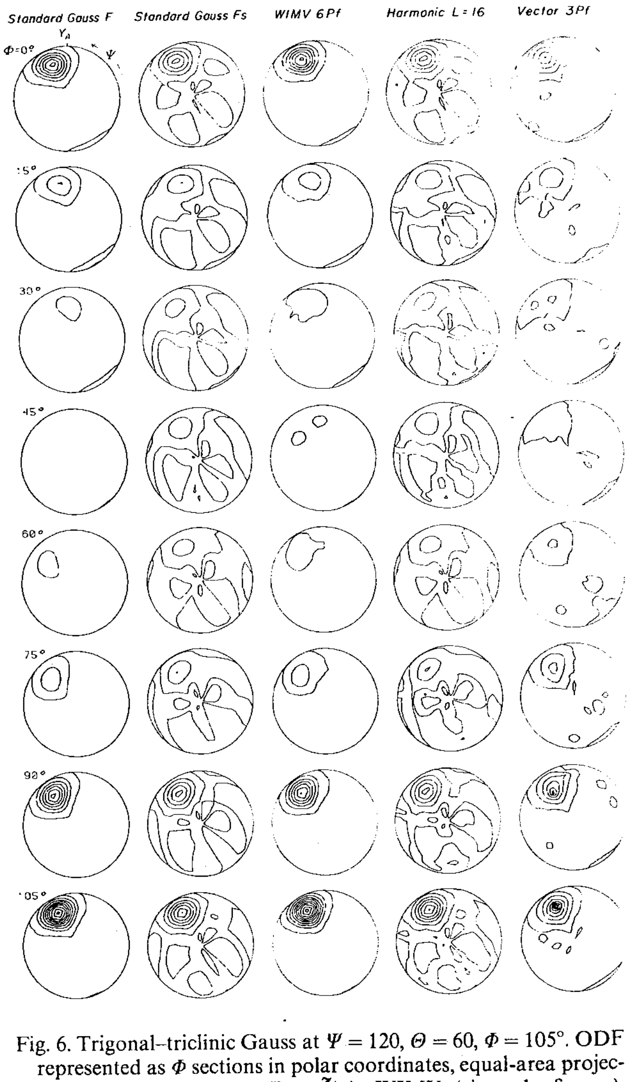

Fig. 6. Trigonal–triclinic Gauss at $\Psi = 120$, $\Theta = 60$, $\Phi = 105°$. ODF represented as Φ sections in polar coordinates, equal-area projection. F is model $f(g)$, Fs $= \tilde{f}(g)$, WIMV (six pole figures), Harmonic (six pole figures), Vector (three pole figures) are ODF's reproduced with the respective methods. The solution for WIMV with three pole figures is visually identical to that for six pole figures. Contours are 0, 1, 3, 5, 7, 9, 11, 13, 15, 17, 19 m.r.d. Negative areas are dotted.

, positive and
not perpendi-
ically different
Wenk, 1985).
another but is
0.6⟩, ⟨10.4⟩,
related by a
stinguishable,
tions. In these
spondingly in-
sis the initial
rst refinement
second phon
improved the

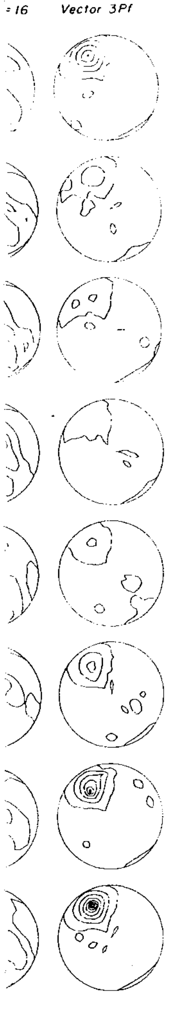

), $\Phi = 105°$. ODF
qual-area projec-
ix pole figures),
gures) are ODF's
lution for WIMV
that for six pole
19 m.r.d. Negative

results slightly. Notice the regular axial symmetry of the Gauss peak in pole figures. This symmetry is commonly distorted by G-space representation, even in the relatively undistorted representation with polar coordinates. It is particularly evident in the peak shape and in the low contour levels of $f(g)$. If one uses a special '$\pi/4$ projection' of the σ sections (Helming *et al.*, 1987), this distortion disappears.

7.2. *Trigonal–orthorhombic symmetry – Taylor* (*Figs.* 7 *and* 8 *and Table* 7)

The previous examples with model distributions constructed by standard functions provided convenient test cases but were highly artificial. In order to investigate a more realistic case we have simulated a texture for calcite polycrystals after plane strain–pure shear deformation with the Taylor theory (Wenk, Takeshita, Van Houtte & Wagner, 1986; Takeshita, Tomé, Wenk & Kocks, 1987). The Taylor calculation used 1440 representative orientations which were smoothed by expressing each orientation with a Gaussian profile of 10° half-width and then expanding the distribution with harmonic functions up to order $L = 16$ (Wagner, Wenk, Esling & Bunge, 1981). Both $f(g) \equiv f^L(g)$ and $\tilde{f}(g) \equiv \tilde{f}^L(g)$ (Fig. 8) show a complicated three-dimensional distribution, far too complex to be expressed with a few standard functions. Only a small region in $f(g)$ is close to zero (0·01), but there are significant negative regions in $\tilde{f}(g)$ ($-0·5$). Note that for trigonal–orthorhombic symmetry Φ sections need only to extend from 30 to 90° and of course a 180° sector in Ψ would be sufficient. We show the full hemisphere to make it easier to compare with the other

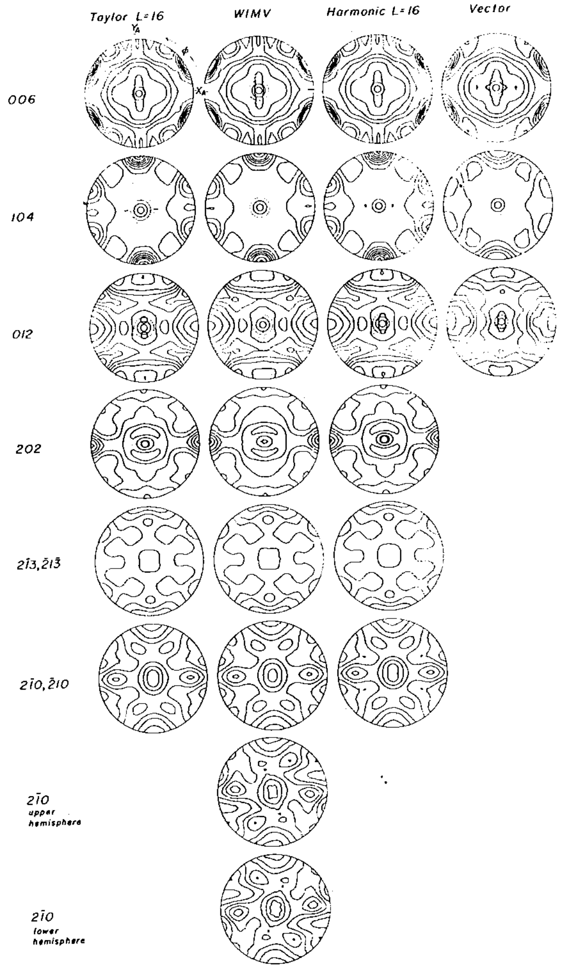

Fig. 7. Trigonal–orthorhombic model texture based on a Taylor simulation for calcite (*cf* Wenk, Takeshita, Van Houtte & Wagner, 1986). Input pole figures (Taylor $L = 16$) are compared with recalculated pole figures using different reproduction methods. X_A is direction of principal compressive strain, Y_A of principal extensive strain. The two bottom diagrams are ideal pole figures $\mathscr{P}_{h_i}(y)$ for $+\langle 2\bar{1}0\rangle$. Equal-area projection, contour interval for 006 is 0·5 m.r.d.; for all others 0·25 m.r.d., dotted below 1 m.r.d.

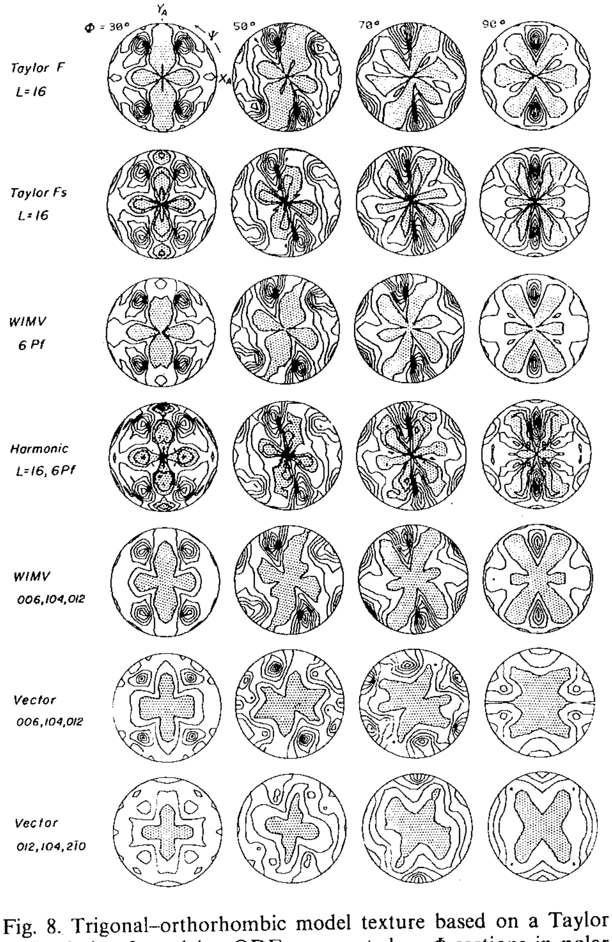

Fig. 8. Trigonal–orthorhombic model texture based on a Taylor simulation for calcite. ODF represented as Φ sections in polar coordinates, equal-area projection. F is model $f(g)$, Fs $= \tilde{f}(g)$, WIMV (three and six pole figures), Harmonic (six pole figures), Vector (three pole figures, two combinations) are ODF's reproduced with the respective methods. X_A is direction of principal compressive strain. Contour intervals are 0·5 m.r.d. Shaded below 0·5 m.r.d.

Table 7. *Error analysis of trigonal–orthorhombic Taylor model*

Pole figures	Method*	I	Maximum	Minimum	RP0 (%)	RP1 (%)
006	Taylor		2·80	0·19		
	W $F=0$	6	2·83	0·20	2·02	1·17
	W $F=0$	3	2·86	0·19	0·80	1·10
	$Hr16$	6	2·79	0·19	0·89	0·15
	$V1$	3	2·44	0·13	15·0	13·0
104	Taylor		2·87	0·52		
	W	6	2·78	0·57	1·97	0·57
	W	3	2·91	0·53	1·63	0·53
	$Hr16$	6	2·86	0·51	0·90	0·51
	$V1$	3	2·61	0·52	8·0	8·2
012	Taylor		1·87	0·14		
	W	6	1·83	0·12	2·64	1·33
	W	3	1·82	0·13	3·08	1·60
	$Hr16$	6	1·86	0·14	1·23	0·25
	$V1$	3	1·52	0·32	13·4	9·8
	$V2$	3	1·51	0·32	13·2	10·9
202	Taylor		2·12	0·46		
	W	6	2·08	0·46	3·52	2·35
	$Hr16$	6	2·12	0·45	0·98	0·37
	$V2$	3	1·71	0·50	8·3	5·5
$2\bar{1}3$	Taylor		1·43	0·54		
	W	6	1·43	0·59	1·65	1·20
	$Hr16$	6	1·37	0·54	0·94	1·22
$2\bar{1}0$	Taylor		1·98	0·38		
	W	6	2·00	0·39	2·05	1·25
	$Hr16$	6	1·86	0·36	1·37	1·64
	$V2$	3	1·90	0·65	14·7	6·8
ODF	Taylor f		4·49	−0·02		
	Taylor $\tilde{f}$		3·94	−0·49		
	W	6	4·95	0·01	2·31	1·57
	W	3	5·10	0·06	1·84	1·22
	$Hr16$	6	3·96	−0·67	1·05	0·64
	$V1$	3	4·48	0·0	12·1	10·3
	$V2$	3	3·82	0·0	12·1	7·7

*Symbols as for Table 5.

trigonal ODF's and to illustrate how symmetry appears in these representations. From the coefficients of the harmonic expansion we have also calculated six pole figures (to $L=16$) which served as input for the analysis (Fig. 7). Since the harmonic apparatus was used to calculate the initial pole figures, the recalculated coefficients [and thus pole figures and $\tilde{f}(g)$] agree closely with coefficients obtained from individual orientations, confirming mainly the internal consistency of all programs and documenting the magnitude of rounding errors.

The vector method using three pole figures yielded unsatisfactory results. This is particularly evident in $f^M(g)$. Whereas peaks are more or less at the correct positions, intensities are off. We see the reason for the lack of resolution in the cell size, which cannot represent this rugged topography. It could only be improved by using a finer discretization of pole figures, which may not be physically meaningful. Some important features, such as the maximum at $\Psi=90$, $\Theta=45$ and $\Phi=90°$, are simply missing.

WIMV with three or six pole figures generates $f^M(g)$ very close to $f(g)$, indicating that WIMV conditions are not only applicable to special model distributions but also to physically meaningful models of texture development by slip. Interestingly, analyses with three and with six pole figures yield almost identical results. RP errors for WIMV are slightly larger than for the harmonic method because the harmonic method simply checked for internal consistency.

Even though the texture shows orthorhombic symmetry, all calculations were done with triclinic sample symmetry, which is the reason for minor deviations from orthorhombic symmetry in the case of the vector method. Wenk, Johnson & Matthies (1988) have illustrated this same example by deconvoluting the WIMV $f^M(g)$ explicitly into $\tilde{f}^M(g)$ and $\tilde{\tilde{f}}^M(g)$. As was shown, $\tilde{\tilde{f}}^M(g)$, which is not implicit in the pole figures, is very close to the corresponding Taylor solution $\tilde{\tilde{f}}(g)$. The reproduction method is therefore significant when Taylor ODF's are compared with ODF's calculated from experimental pole figure. The maximum in the WIMV ODF (4·95) is slightly exaggerated over $f(g)$ (4·5) owing to the WIMV condition of maximum texture index, and much higher than the maximum in $\tilde{f}(g)$ (3·9).

7.3. *Actual measurements* (*ODF unknown*) (*Figs.* 9–11, *Table* 8).

The first column of Fig. 9 shows pole figures of an experimentally deformed limestone which were measured by neutron and X-ray diffraction. The sample K338 was deformed in plane strain–pure shear at 673 K (Wenk, Kern & Wagner, 1981) and displays approximately orthorhombic sample symmetry, but no symmetry was assumed in the calculations. Three pole figures (00.6), (10.4) and (01.2) were measured on a 1 cm^3 cube by neutron diffraction, another two, (20.2) and (2$\bar{1}$.3), on a small area of a slab cut through the central part of the sample with X-ray diffraction in reflection geometry. Since there is some sample heterogeneity – the central part (X-ray) shows stronger preferred orientation than the average over a large volume (neutron) – the combination of the two data sets causes problems. This will become apparent in the ODF reproduction. The example is not an optimal data set but is useful to demonstrate error analysis for real data.

In this case the true ODF is obviously unknown. We can only assume that similar differences exist between $f(g)$ and $\tilde{f}(g)$ as in the case of Taylor because similar mechanisms and a similar strain history were assumed in the simulation and in this experiment (Takeshita *et al.*, 1987). A glance at Table 8 illustrates that RP values range between 5 and 10% rather than between 0·5 and 1% as in the previous examples. The three neutron pole figures were analyzed with WIMV and vector methods. The excellent resolution of WIMV is demonstrated in the pole-figure comparisons (Fig. 9). Compare, for example, $\tilde{P}_{006}$ with $\tilde{P}^{M}_{006}$, which agree within minor details such as slight deviations from orthorhombic symmetry. Resolution with the vector method, using the same data, is much less satisfactory.

In the conventional harmonic method three pole figures are only enough to expand to $L = 6$, which cannot resolve any details. Therefore we used five pole figures and $L = 12$, and obtained similar RP values to WIMV method with the same five pole figures. But RP values for five pole figures are much higher than for three. We attribute this to incompatibility of neutron and X-ray pole figures. Recalculated pole figures are consistently weaker than the experimental X-ray pole figures which were measured in the central part of the specimen with the strongest preferred orientation. This is well documented with difference pole figures (measured − calculated) (Fig. 11) in which positive peaks appear for X-ray and negative deviations for neutron pole figures. Interestingly, three- and five-pole-figure WIMV ODF's are similar (Fig. 10) and compare well with the Taylor prediction for similar deformation conditions (Fig. 8), as do ideal pole figures for $\langle 2\bar{1}0\rangle$, which lack an inversion center (Fig. 9). The harmonic method reproduces qualitatively the principal features but with much noise. Since negative areas are insignificant, the positivity condition alone could not remedy the situation. The vector method with these real data for a complex texture fails to resolve the ODF.

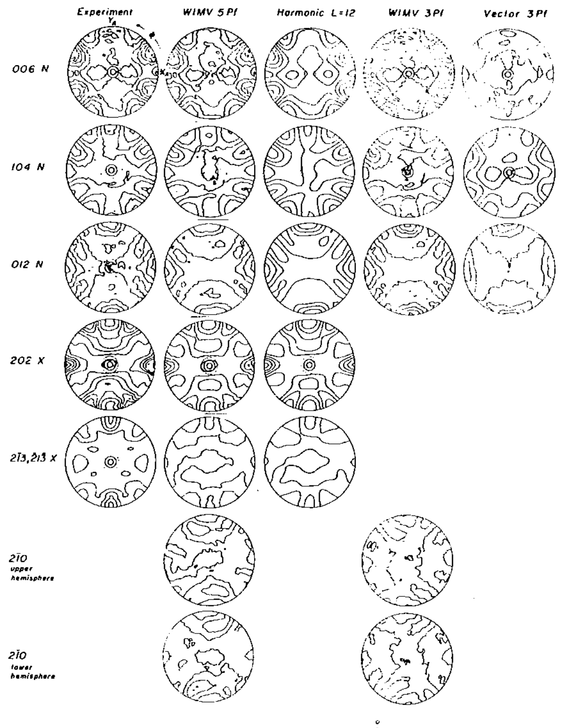

Fig. 9. Trigonal–triclinic texture of experimentally deformed limestone K338 (Wenk, Kern & Wagner, 1981). Pole figures measured by neutron (N) and X-ray diffraction (X) are compared with recalculated pole figures using different reproduction methods. X_A is direction of principal compressive strain. The two bottom diagrams are ideal pole figures $\mathscr{P}_{\mathbf{h}_i}(\mathbf{y})$ for $+\langle 2\bar{1}0\rangle$. Equal-area projection, contour interval is 0·5, dotted below 1 m.r.d.

8. Concluding remarks

The first part of this paper summarizes the most important aspects of quantitative texture analysis, particularly in view of the loss of information if the ODF is reproduced from pole figures. In recent years, with increasing popularity of quantitative texture

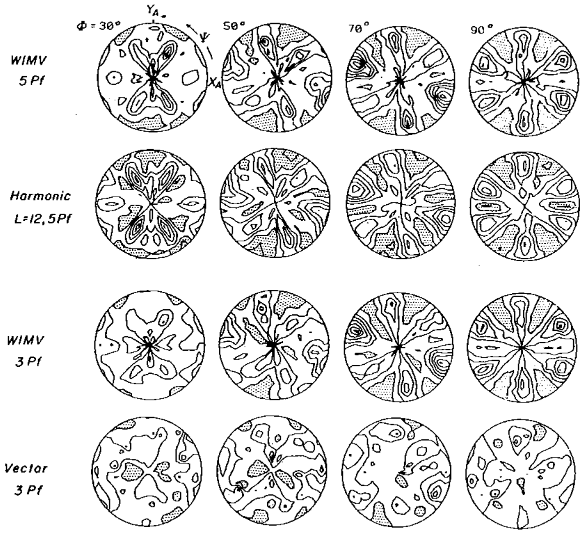

Fig. 10. Trigonal–triclinic texture of experimentally deformed limestone K338. ODF represented as Φ sections in polar coordinates, equal-area projection. F is model $f(g)$, Fs $=\tilde{f}(g)$, WIMV (three and five pole figures), Harmonic (five pole figures), Vector (three pole figures) are ODF's reproduced with the respective methods. X_A is direction of principal compressive strain. Contour intervals are 0·5 m.r.d. Shaded below 0·5 m.r.d.

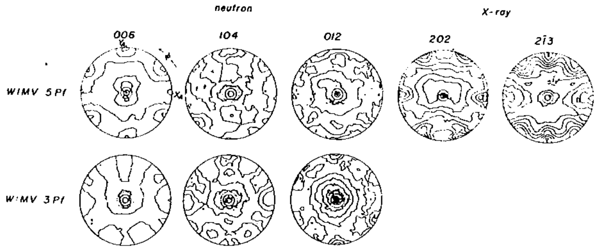

Fig. 11. Difference pole figures (experimental − calculated) for texture shown in Figs. 9 and 10, reproduced by WIMV (three and five pole-figure fit), illustrate incompatibility of neutron and X-ray pole figures due to sample heterogeneity. Large positive deviations are apparent in the X-ray pole figures. Contour intervals are 0·1 m.r.d.; negative areas are dotted.

Table 8. *Error analysis of experimentally deformed limestone texture,* K338 (*three neutron and two X-ray pole figures*)

Pole figures	Method*	l	Maximum	Minimum	RP0 (%)	RP1 (%)
006	Neutron		2·06	0·22		
	W	5	1·88	0·21	10·0	5·8
	W	3	2·01	0·22	2·7	1·9
	*H*12	5	1·93	0·20	8·4	4·7
	V	3	2·44	0·20	8·5	7·2
104	Neutron		1·70	0·46		
	W	5	1·63	0·48	6·6	4·0
	W	3	1·59	0·50	4·6	2·8
	*H*12	5	1·66	0·41	7·3	8·0
	V	3	1·71	0·04	11·0	10·0
012	Neutron		1·73	0·40		
	W	5	1·78	0·42	7·3	6·3
	W	3	1·81	0·39	7·1	6·1
	*H*12	5	1·72	0·38	8·1	8·7
	V	3	1·41	0·38	8·8	7·8
202	X-ray		2·49	0·43		
	W	5	2·00	0·61	19·4	9·4
	*H*12	5	1·87	0·52	23·1	11·7
$2\bar{1}3$	X-ray		1·86	0·71		
	W	5	1·37	0·72	17·5	12·9
	*H*12	5	1·39	0·72	17·2	14·0
ODF	*W*	5	4·57	0·19	12·2	7·7
	W	3	4·38	0·20	4·8	3·6
	*H*12	5	3·27	−0·43	12·8	9·4
	V	3	3·35	0·0	9·4	8·3

*Symbols as for Table 5.

analysis, both in materials science and geology, considerable diversity has developed in conventions, mathematical procedures, representation, and error evaluation, which can cause confusion as texture analysis is applied more and more to low-symmetry materials. It is clear that more uniformity would be very desirable, particularly for applications of texture data. We make some recommendations about the choice of Euler angles, crystal coordinates, ODF representation and error criteria which appear to be a useful basis for further discussions.

In the second part we use the recommended procedure to analyse several test examples with the conventional harmonic, vector and WIMV methods. We find in the numerical results considerable agreement with the intrinsic properties of each method.

The conventional harmonic method reproduces the ghost-afflicted reduced ODF $\tilde{f}(g)$ with good quality and relatively little computational effort. Resolution is limited by series termination (L) and to some extent by the integration algorithm used to calculate F coefficients. If nonlinear conditional ghost corrections are introduced, the computational effort increases and requires an iterative approach. Zero ranges in pole figures often do not exist and are difficult to define and therefore the corresponding ghost-correction method is not applicable. For low crystal symmetry the number of required pole figures to obtain a high enough expansion (at least $L = 16$ is generally desirable) is often beyond the number which can be satisfactorily measured owing to frequent peak overlaps at low symmetry (Wenk, Bunge, Jansen & Pannetier, 1986). A main advantage of the harmonic method is the elegant representation of macroscopic physical properties (Bunge, 1969), needing for their calculation a small number of coefficients, $C_l^{\mu,\nu}$, only.

For WIMV the resolution is much less dependent on the number of pole figures because the method in a maximum way makes use of experimental information contained in each pole figure. Rather surprisingly, single-pole-figure fits often reproduce $f(g)$ with good accuracy, but clearly more pole figures are desirable to ascertain consistency. The small number of required pole figures offers a definite advantage for low crystal symmetry. Also, in an on-line metallurgical production environment a minimum amount of experimental measurements can be a crucial factor. WIMV, with its assumptions of maximum background and smooth peak shape, is able to resolve $f(g)$ not only for model distributions constructed by standard functions but also for Taylor predictions and therefore seems to be most suitable for deformation textures. The computer effort is considerable and requires large arrays which relate cells in ODF and pole-figure space. The result of WIMV is a three-dimensional density distribution, but from this array Fourier coefficients $C_l^{\mu,\nu}$, both even and odd, can easily be calculated and used to obtain properties in an effective manner. Alternatively, physical properties can be calculated directly from weighted averaging over the ODF array (Wenk, Johnson & Matthies, 1988). Even though we have not demonstrated this here, WIMV is also well suited to treat incomplete pole figures because the product approach makes normalization straightforward.

The vector method, with the ingenious principle of a linear relationship between cells in pole-figure and ODF space, is the most transparent of all three methods and produces $f^M(g) \geq 0$; however, it is severely limited by the requirement that there need to be more cells in pole-figure space than in G space, resulting in large volume elements which average over large regions in the ODF. For cubic–orthorhombic symmetry the vector method produces a semiquantitative solution which is (for missing pole-figure zeros) close to $\tilde{f}(g)$ with its reduced peak maxima and ghost components. For trigonal–triclinic symmetry we have failed to obtain satisfactory results. Moreover, the method is most demanding of computer resources.

Harmonic and WIMV methods are equally quantitative as measured by RP values. Pole figures with RP values of less than 2% represent an almost perfect match close to the internal resolution of the method. RP values between 2 and 5% are expected for good measurements, and an average RP of less than 5% is representative of a good reproduction. On the other

desirable) is
satisfactorily
rlaps at low
netier, 1986).
ethod is the
physical pro-
calculation a

ss dependent
e method in a
l information
surprisingly,
g) with good
e desirable to
r of required
or low crystal
gical produc-
experimental
IMV, with its
and smooth
nly for model
functions but
e seems to be
The computer
arrays which
. The result of
distribution,
both even
sed to obtain
atively, phys-
directly from
array (Wenk,
h we have not
well suited to
the product
forward.
s principle of a
le-figure and
of all three
ever, it is sev-
there need to
n in G space,
h average over
orthorhombic
s a semiquan-
g pole-figure
k maxima and
c symmetry we
lts. Moreover,
uter resources.
equally quan-
le figures with
almost perfect
of the method.
ected for good
ess than 5% is
. On the other

hand, if RP exceeds 10% this indicates some deficiency, and difference pole figures are necessary to identify the problem, which may be sample heterogeneity, error in data correction, a relative rotation error, or simply counting statistics. A poor RP value does not necessarily indicate that the data are worthless, particularly if pole figures display strong peaks. For publication purposes, we recommend showing measured pole figures and difference pole figures in addition to ODF's. The latter display systematic errors more transparently than recalculated figures. The intrinsic resolution of WIMV and harmonic methods is about a factor of 2–5 better than errors introduced even by the best experimental pole-figure data which are presently available, and we recommend that more effort should now be directed towards measuring truly quantitative pole figures and assessing uncertainties in the data. Some efforts at standardization are presently under way (*e.g.* Wenk, Kern, Pannetier, Höfler, Schäfer, Will & Brokmeier, 1987).

We acknowledge support through grants NSF EAR 84–06070, IGPP-LANL and IBM-DACE. SM is appreciative for support and excellent working conditions during his Berkeley leave in fall 1985. HRW thanks the A. v. Humboldt Foundation for supporting leaves in Germany in 1984 and 1987. H. Schaeben, A. Vadon and F. Wagner kindly provided computer codes which were used in this work. C. Esling and F. Wagner (Metz) made available data for cubic staircase integrations and offered many useful comments. Constructive comments by reviewers helped to improve the manuscript.

References

BECHLER-FERRY, E., WAGNER, F., HUMBERT, M., ESLING, C. & BARO, R. (1981). In *Proceedings of 6th International Conference on Textures of Materials, Tokyo*, edited by S. NAGASHIMA, pp. 1300–1309. The Iron and Steel Institute of Japan, Tokyo.

BUNGE, H. J. (1969). *Mathematische Methoden der Texturanalyse.* Berlin: Akademieverlag.

BUNGE, H. J. (1982). *Texture Analysis in Materials Science.* London: Butterworths.

BUNGE, H. J. (1987). In *Proceedings of 8th International Conference on Textures of Materials, Santa Fe*, edited by J. S. KALLEND & G. GOTTSTEIN. Warrendale, PA: TMS. In the press.

BUNGE, H. J. & ESLING, C. (1979). *J. Phys. (Paris)*, **40**, 627–628.

BUNGE, H. J. & ESLING, C. (1981). *J. Appl. Cryst.* **14**, 253–255.

BUNGE, H. J. & ESLING, C. (1982). Editors. *Quantitative Texture Analysis.* Oberursel: Deutsche Gesellschaft für Metallkunde e.V.

BUNGE, H. J. & ESLING, C. (1985). In *Preferred Orientation in Deformed Metals and Rocks. An Introduction to Modern Texture Analysis*, edited by H. R. WENK, pp. 109–122. Orlando, FL: Academic Press.

DAHMS, M. & BUNGE, H. J. (1986). *Textures Microstruct.* **6**, 167–179.

EDMONDS, A. R. (1957). *Angular Momentum in Quantum Mechanics.* Princeton Univ. Press.

HAHN, T. (1983). Editor. *International Tables for Crystallography*, Vol. A. Dordrecht: Reidel.

HAUSSÜHL, S. (1983). *Kristallphysik.* Weinheim: Physik-Verlag.

HELMING, K. & MATTHIES, S. (1984). *Phys. Status Solidi B*, **126**, 43–52.

HELMING, K., MATTHIES, S. & VINEL, G. (1987). In *Proceedings of 8th International Conference on Textures of Materials, Santa Fe*, edited by J. S. KALLEND & G. GOTTSTEIN. Warrendale, PA: TMS. In the press.

HUMBERT, M. (1976). Thesis. Univ. of Metz, France.

HUMPHREYS, F. J. (1983). *Textures Microstruct.* **6**, 45–61.

IMHOF, J. (1977). *Z. Metallkd.* **68**, 38–43.

IMHOF, J. (1982). *Textures Microstruct.* **5**, 73–86.

JURA, J., POSPIECH, J. & BUNGE, H. J. (1976). *Pol. Akad. Nauk Metal.* **24**, 111–176.

JURA, J., POSPIECH, J. & LÜCKE, K. (1980). *Z. Metallkd.* **71**, 714–728.

KOCKS, U. F. (1987). In *Proceedings of 8th International Conference on Textures of Materials, Santa Fe*, edited by J. S. KALLEND & G. GOTTSTEIN. Warrendale, PA: TMS. In the press.

LEE, H. P., BUNGE, H. J. & ESLING, C. (1986). *Textures Microstruct.* **6**, 289–313.

LIANG, Z., WANG, F. & XU, J. (1987). In *Proceedings 8th International Conference on Textures of Materials, Santa Fe*, edited by J. S. KALLEND & G. GOTTSTEIN. Warrendale, PA: TMS. In the press.

LÜCKE, K., POSPIECH, J., JURA, J. & HIRSCH, J. (1986). *Z. Metallkd.* **77**, 312–321.

MATTHIES, S. (1979). *Phys. Status Solidi B*, **92**, K135–K138.

MATTHIES, S. (1980*a*). *Kristall Tech.* **15**, 431–444.

MATTHIES, S. (1980*b*). *Phys. Status Solidi B*, **101**, K111–K115.

MATTHIES, S. (1981). *Cryst. Res. Tech.* **16**, 1061–1071.

MATTHIES, S. (1982*a*). *Aktuelle Probleme der Quantitativen Texturanalyse.* Dresden: Akademie der Wissenschaften der DDR, Zentralinstitut für Kernforschung Rossendorf.

MATTHIES, S. (1982*b*). *Phys. Status Solidi B*, **112**, 705–716.

MATTHIES, S. (1984). *Proceedings of 7th International Conference on Textures of Materials, Noordwijkerhout*, edited by C. M. BRAKMAN, P. JONGENBURGER & E. J. MITTEMEIJER, pp. 737–751. Amsterdam: Netherlands Society for Materials Science.

MATTHIES, S. (1986). *Ann. Phys.* **43**, 299–306.

MATTHIES, S. & HELMING, K. (1982). *Phys. Status Solidi B*, **113**, 569–582.

MATTHIES, S. & VINEL, G. W. (1982). *Phys. Status Solidi B*, **112**, K111–K120.

MATTHIES, S., VINEL, G. W. & HELMING, K. (1987). *Standard Distributions in Texture Analysis*, Vol. 1. Berlin: Akademieverlag.

MATTHIES, S. & WAGNER, F. (1981). *Phys. Status Solidi B*, **107**, 591–601.

MATTHIES, S. & WENK, H. R. (1985). In *Preferred Orientation in Deformed Metals and Rocks. An Introduction to Modern Texture Analysis*, edited by H. R. WENK, pp. 139–147. Orlando, FL: Academic Press.

NYE, J. F. (1957). *Physical Properties of Crystals.* Oxford Univ. Press.

OERTEL, G. (1985). In *Preferred Orientation in Deformed Metals and Rocks. An Introduction to Modern Texture Analysis*, edited by H. R. WENK, pp. 431–440. Orlando, FL: Academic Press.

PAWLIK, K. (1986). *Phys. Status Solidi B*, **134**, 477–483.

POSPIECH, J. (1982). *Quantitative Texture Analysis*, edited by H. J. BUNGE & C. ESLING, p. 239–317. Oberursel: Deutsche Gesellschaft für Metallkunde e.V.

POSPIECH, J. (1987). In *Proceedings of 8th International Conference on Textures of Materials, Santa Fe*, edited by J. S. KALLEND & G. GOTTSTEIN. Warrendale, PA: TMS. In the press.

ROE, R. J. (1965). *J. Appl. Phys.* **36**, 2024–2031.

RUER, D. (1976). *Méthode Vectorielle d'Analyse de la Texture.* Thesis. Univ. of Metz, France.

RUER, D. & BARO, R. (1977). *J. Appl. Cryst.* **10**, 458–464.

SCHAEBEN, H. (1984). *Phys. Status Solidi B*, **123**, 425–434.

SCHAEBEN, H., VADON, A. & WENK, H. R. (1985). In *Preferred Orientation in Deformed Metals and Rocks. An Introduction to Modern Texture Analysis*, edited by H. R. WENK, pp. 123–137. Orlando, FL: Academic Press.

TAKESHITA, T., TOMÉ, C., WENK, H. R. & KOCKS, F. U. (1987). *J. Geophys. Res.* **92***B*, 12917–12930.

TAYLOR, G. I. (1938). *J. Inst. Met.* **62**, 307–324.

VADON, A. (1981). *Generalisation et Optimisation de la Methode Vectorielle d'Analyse de la Texture.* Thesis. Univ. of Metz, France.

VAN HOUTTE, P. (1983). *Textures Microstruct.* **6**, 1–19.

VARSHALOVIC, D. A., MOSKALEV, A. N. & CHERSONSKIJ, V. K. (1975). *Kvantovaja Teorija Uglovogo Momenta.* Leningrad: Izd. Nauka.

WAGNER, F. (1984). Thesis. Univ. of Metz, France.

WAGNER, F., WENK, H. R., ESLING, C. & BUNGE, H. J. (1981). *Phys. Status Solidi A*, **67**, 269–285.

WASSERMANN, G. & GREWEN, J. (1962). *Texturen metallischer Werkstoffe.* Berlin: Springer-Verlag.

WEISS, L. E. & WENK, H. R. (1985). In *Preferred Orientation in Deformed Metals and Rocks. An Introduction to Modern Texture Analysis*, edited by H. R. WENK, pp. 49–72. Orlando, FL: Academic Press.

WENK, H. R. (1985). Editor. *Preferred Orientation in Deformed Metals and Rocks: An Introduction to Modern Texture Analysis.* Orlando, FL: Academic Press.

WENK, H. R., BUNGE, H. J., JANSEN, E. & PANNETIER, J. (1986). *Tectonophysics*, **126**, 271–284.

WENK, H. R., BUNGE, H. J., KALLEND, J. S., LÜCKE, K., MATTHIES, S., POSPIECH, J. & VAN HOUTTE, P. (1987). In *Proceedings of 8th International Conference on Textures of Materials, Santa Fe*, edited by J. S. KALLEND & G. GOTTSTEIN. Warrendale, PA: TMS. In the press.

WENK, H. R., JOHNSON, G. J. & MATTHIES, S. (1988). *J. Appl. Phys.* In the press.

WENK, H. R., KERN, H., PANNETIER, J., HÖFLER, S., SCHÄFER, W., WILL, G. & BROKMEIER, H.-G. (1987). In *Proceedings of 8th International Conference on Texture of Materials, Santa Fe*, edited by J. S. KALLEND & G. GOTTSTEIN. Warrendale, PA: TMS. In the press.

WENK, H. R., KERN, H. & WAGNER, F. (1981). *Deformation of Polycrystals: Mechanisms and Microstructures*, pp. 235–245. Roskilde, Denmark: Risø National Laboratory.

WENK, H. R. & KOCKS, U. F. (1987). *Metall. Trans.* **18A**, 1083–1092.

WENK, H. R., O'BRIEN, D. & YOU, Z. (1985). *Phys. Status Solidi A*, **90**, K19–K24.

WENK, H. R., TAKESHITA, T., VAN HOUTTE, P. & WAGNER, F. (1986). *J. Geophys. Res.* **91**, 3861–3869.

WENK, H. R. & WILDE, W. R. (1972). *Am. Geophys. U. Monogr.* **16**, 84–94.

WILLIAMS, R. D. (1968). *J. Appl. Phys.* **39**, 4329–4335.